

---

# Memory-Efficient Orthogonal Fine-Tuning with Principal Subspace Adaptation

---

**Fei Wu**  
University of Exeter  
fw407@exeter.ac.uk

**Jia Hu**  
University of Exeter  
j.hu@exeter.ac.uk

**Geyong Min**  
University of Exeter  
g.min@exeter.ac.uk

**Shiqiang Wang**  
IBM T. J. Watson Research Center  
wangshiq@us.ibm.com

## Abstract

Driven by the relentless growth in model parameters—which renders full fine-tuning prohibitively expensive for large-scale deployment—parameter-efficient fine-tuning (PEFT) has emerged as a crucial approach for rapidly adapting large models to a wide range of downstream tasks. Among the PEFT family, orthogonal fine-tuning and its variants have demonstrated remarkable performance by preserving hyperspherical energy, which encodes pairwise angular similarity between neurons. However, these methods are inherently memory-inefficient due to the need to store intermediate activations from multiple full-dimensional sparse matrices. To address this limitation, we propose Memory-efficient Orthogonal Fine-Tuning (MOFT) with principal subspace adaptation. Specifically, we first establish a theoretical condition under which orthogonal transformations within a low-rank subspace preserve hyperspherical energy. Based on this insight, we constrain orthogonal fine-tuning to the principal subspace defined by the top- $r$  components obtained through singular value decomposition and impose an additional constraint on the projection matrix to satisfy the preservation condition. To enhance MOFT’s flexibility across tasks, we relax strict orthogonality by introducing two learnable scaling vectors. Extensive experiments on 37 diverse tasks and four models across NLP and CV demonstrate that MOFT consistently outperforms key baselines while significantly reducing the memory footprint of orthogonal fine-tuning.

## 1 Introduction

Pre-trained foundation models such as the LLaMA-3 series [1] and ViT [2] have demonstrated remarkable generalization capabilities across domains, including natural language processing (NLP) [3] and computer vision (CV) [4]. This success is attributed to emergent abilities [5] that arise from scaling up these models. However, the growing number of parameters poses a significant challenge in tailoring (*i.e.*, fine-tuning) these sophisticated foundation models to specific downstream tasks. To address this challenge, parameter-efficient fine-tuning (PEFT) has emerged as an effective approach that fine-tunes only a minimal subset of parameters [6–10]. Among PEFT studies, reparameterization-based methods [9, 11] are widely adopted for their seamless integration into pre-trained models without adding additional inference latency.

Reparameterization-based methods operate by amplifying or suppressing specific features within the latent space of pre-trained models [9]. As illustrated in the left panel of Figure 1a, these methods fall into two categories: additive and multiplicative fine-tuning. Additive methods, such as Low-Rank Adaptation (LoRA) [9] and its variants [10, 12], inject zero-initialized low-rank modules whose

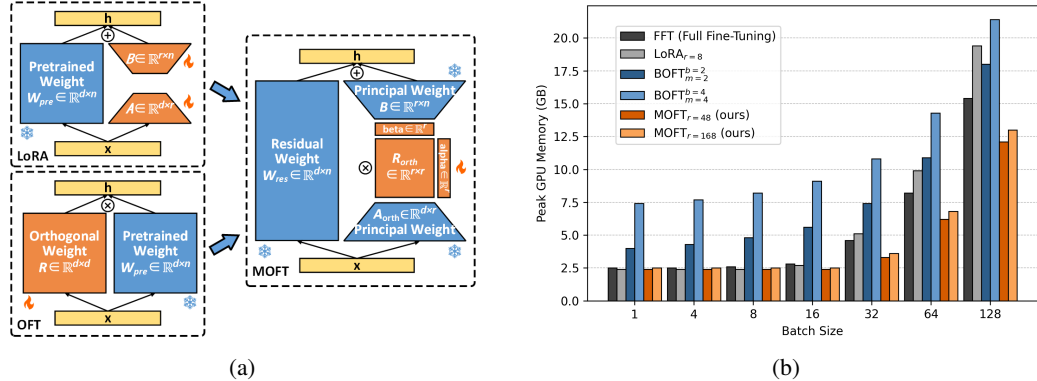


Figure 1: (a) Overview of the proposed MOFT, which constrains orthogonal transformations within the principal subspace and extends flexibility via two scaling vectors. (b) Peak memory usage under varying batch sizes for different fine-tuning methods using the ViT-B/16 model [2] on VTAB-1K [16].

outputs are added to the pre-trained weights, ensuring minimal deviation from the backbone. In contrast, multiplicative methods like Orthogonal Fine-Tuning (OFT) [11] multiply identity-initialized orthogonal modules with pre-trained weights to preserve the relational structure between neurons. OFT [11] mitigates the significant resource demands of full-dimensional orthogonal fine-tuning by employing a block-diagonal structure, albeit at the cost of reduced expressiveness.

Recent works such as BOFT [13] and qGOFT [14] improve parameter efficiency in orthogonal fine-tuning by decomposing dense orthogonal matrices into sparse multiplications without sacrificing expressiveness. For example, BOFT outperforms LoRA by 1.4% on GLUE [15] and 1.3% on VTAB-1K [16] with much fewer parameters [13]. Nevertheless, these methods remain memory-inefficient. Figure 1b shows that BOFT consistently incurs much higher peak memory usage than other methods. Our experiments reveal that GOFT [14] consumes  $2.8\times$  more memory than LoRA on CoLA [15] with DeBERTaV3-large [17], and fine-tuning LLaMA-3.2-3B [18] with BOFT or qGOFT exceeds 80 GB. Such overhead inflates costs and limits practicality, raising a key question: **How can we retain the performance benefits of orthogonal fine-tuning while minimizing memory usage?**

Our analysis in Appendix D reveals that BOFT [13] and qGOFT [14] incur increased activation memory due to the use of multiple full-dimensional sparse matrices. Given evidence that pre-trained models and their task-specific adaptations lie in a low intrinsic rank [19, 20, 9], we hypothesize that orthogonal fine-tuning can be confined to a low-dimensional subspace. Thus, we propose **Memory-Efficient Orthogonal Fine-Tuning (MOFT)** with principal subspace adaptation. As illustrated in the right panel of Figure 1a, the pre-trained weights can be decomposed into principal and residual components, enabling orthogonal transformations to operate directly within the principal subspace. However, we observe that inserting an orthogonal matrix  $R$  alone fails to preserve hyperspherical energy unless  $A^\top A$  and  $R$  commute, where  $A$  denotes the projection matrix. To satisfy this condition, we enforce  $A^\top A = I_r$  when constructing the principal subspace. We further improve MOFT’s adaptability by relaxing strict orthogonality through two learnable scaling vectors.

We evaluate MOFT on 37 tasks across NLP and CV using four representative pre-trained models. MOFT consistently outperforms key baselines, yielding notable gains over advanced OFT methods: **+3.3** on commonsense reasoning (LLaMA-3.1-8B), **+5.8** on mathematical QA (LLaMA-3.2-3B), **+0.2** on natural language understanding (DeBERTaV3-base), and **+3.3** on visual classification (ViT-B/16). It also achieves an average peak memory reduction of **43.4%**, with the maximum reaching nearly **70%**. As shown in Figure 1b, MOFT incurs lower memory overhead than prior OFT methods, and its advantage over full fine-tuning and LoRA becomes more pronounced as batch size increases.

We summarize our contributions as follows:

- We establish a theoretical condition under which orthogonal transformations within a low-rank subspace preserve hyperspherical energy, thereby bridging the gap between orthogonal fine-tuning and low-rank adaptation.
- We propose MOFT, a novel PEFT framework that confines orthogonal fine-tuning to the principal subspace and introduces a constraint on the down-projection matrix. We further enhance its flexibility by relaxing the requirement of strict orthogonality.

- We conduct extensive experiments across NLP and CV tasks with diverse model architectures, demonstrating that MOFT consistently outperforms key baselines while reducing the memory overhead of orthogonal fine-tuning to a level comparable to LoRA.

## 2 Related Work

**Parameter-Efficient Fine-Tuning (PEFT).** PEFT adapts pre-trained models to diverse downstream tasks by fine-tuning only a small subset of parameters. Existing PEFT methods fall into three categories: **1) Selection-based** methods select specific components of the pre-trained model without altering its architecture [21–23]. **2) Addition-based** methods insert *prompts* or *adapters* at the input or within Transformer blocks [8, 24, 7, 6, 25]. **3) Reparameterization-based** methods reparameterize weights in parallel with minimal parameters [9, 26, 10, 12, 27–29]. Reparameterization-based methods are widely adopted for incurring no additional inference latency, with representative examples including LoRA [9] and OFT [11]. PiSSA [12] improves convergence by modifying LoRA’s initialization, while the proposed MOFT aligns initialization with orthogonal fine-tuning and tunes only the orthogonal matrix inserted between the low-rank components.

**Orthogonal Fine-Tuning.** Different from LoRA, orthogonal fine-tuning enhances performance by preserving hyperspherical energy among neurons [30, 11]. OFT [11] adopts a block-diagonal sparsity structure to reduce the computational cost, although this structure may introduce undesired inductive biases [13]. BOFT [13] and qGOFT [14] address this issue by replacing dense matrices with sequences of sparse matrix multiplications, thereby improving parameter efficiency while preserving model expressiveness. Despite their empirical effectiveness, these methods remain memory-inefficient compared to LoRA and its variants. Recent work such as Adapter<sup>R</sup> [31] performs orthogonal fine-tuning by rotating two sets of singular vectors from spectral decomposition. In contrast, the proposed MOFT applies a single orthogonal transformation within the principal subspace. LaMDA [32] and LoRA-XS [29] adopt a structure similar to MOFT but they do not preserve hyperspherical energy, whereas MOFT establishes a theoretical condition to bridge this gap.

## 3 Preliminaries

Conventional full fine-tuning (FFT) updates the entire weight matrix  $\mathbf{W} \in \mathbb{R}^{d \times n}$ , resulting in a small deviation from the pre-trained weights  $\mathbf{W}^{\text{pre}}$ . In contrast, LoRA [9] constrains this deviation to a low-rank subspace, *i.e.*,  $\text{rank}(\mathbf{W} - \mathbf{W}^{\text{pre}}) = r$ , where  $r \ll \min(d, n)$ . Orthogonal fine-tuning [11] instead minimizes the discrepancy in hyperspherical energy between  $\mathbf{W}$  and  $\mathbf{W}^{\text{pre}}$ :

$$\min_{\mathbf{W}} \|\text{HSE}(\mathbf{W}) - \text{HSE}(\mathbf{W}^{\text{pre}})\| \iff \min_{\mathbf{W}} \left\| \sum_{i \neq j} \|\hat{\mathbf{w}}_i - \hat{\mathbf{w}}_j\|^{-1} - \sum_{i \neq j} \|\hat{\mathbf{w}}_i^{\text{pre}} - \hat{\mathbf{w}}_j^{\text{pre}}\|^{-1} \right\|, \quad (1)$$

where  $\text{HSE}(\mathbf{W}) := \sum_{i \neq j} \|\hat{\mathbf{w}}_i - \hat{\mathbf{w}}_j\|^{-1}$  denotes the hyperspherical energy of  $\mathbf{W} = \{\mathbf{w}_1, \dots, \mathbf{w}_n\}$ , with each  $\mathbf{w}_i \in \mathbb{R}^d$  representing the  $i$ -th neuron and  $\hat{\mathbf{w}}_i := \mathbf{w}_i / \|\mathbf{w}_i\|$  its normalized direction.

Equation 1 illustrates the principle of orthogonal fine-tuning, which aims to **preserve pairwise angular similarity between neurons**. This can be achieved by applying a rotation or reflection to the weight matrix,  $\mathbf{W} = \mathbf{R}\mathbf{W}^{\text{pre}}$ , where  $\mathbf{R} \in \mathbb{R}^{d \times d}$  is orthogonal. Given input  $\mathbf{x} \in \mathbb{R}^d$ , the output is:

$$\mathbf{h} = \mathbf{W}^\top \mathbf{x} = (\mathbf{R}\mathbf{W}^{\text{pre}})^\top \mathbf{x}, \quad \text{s.t.} \quad \mathbf{R}^\top \mathbf{R} = \mathbf{R}\mathbf{R}^\top = \mathbf{I}_d, \quad (2)$$

where  $\mathbf{R} \in O(d)$  and  $\mathbf{I}_d$  is the identity matrix. To reduce parameter overhead, OFT [11] constrains  $\mathbf{R}$  to a block-diagonal form, *i.e.*,  $\mathbf{R} = \text{diag}(\mathbf{R}_1, \dots, \mathbf{R}_r)$  with  $\mathbf{R}_r \in O(d/r)$ , which improves efficiency but limits expressiveness due to inductive bias [13]. To address this, BOFT [13] and qGOFT [14] factorize  $\mathbf{R}$  into a product of sparse matrices:  $\mathbf{R} = \prod_{m=1}^{\log d} \tilde{\mathbf{R}}_m$ , where each sparse  $\tilde{\mathbf{R}}_m \in \mathbb{R}^{d \times d}$ , restoring the expressiveness of dense rotations with minimal parameter cost. However, as noted in Section 1, BOFT and qGOFT incur high memory costs from multiple full-dimensional sparse matrices. We introduce an alternative in the next section to address this limitation.

## 4 Methodology

Inspired by prior work [19, 20, 9] showing that both pre-trained models and their task-specific adaptations reside in a low intrinsic rank subspace, we hypothesize that orthogonal fine-tuning can be effectively restricted to such a subspace rather than the full space used in prior methods [11, 13, 14]. This may directly reduce computational and memory costs by lowering the effective dimensionality.

Therefore, we explore preserving hyperspherical energy (*i.e.*, the angular similarity between neurons) within a low-rank subspace. Since directly applying low-dimensional orthogonal transformations to the full-dimensional pre-trained weights  $\mathbf{W}^{\text{pre}}$  is infeasible due to dimensional mismatch, we first project  $\mathbf{W}^{\text{pre}}$  onto a low-rank subspace, and then perform orthogonal fine-tuning within it.

PiSSA [12] provides an efficient way to extract the low-rank subspace. Specifically,  $\mathbf{W}^{\text{pre}}$  is decomposed via Singular Value Decomposition (SVD) as  $\mathbf{W}^{\text{pre}} = \mathbf{U}\mathbf{\Sigma}\mathbf{V}^\top$ , and partitioned into a principal component  $\mathbf{W}^{\text{pri}}$  and a residual  $\mathbf{W}^{\text{res}}$ . The principal component is reconstructed from the top- $r$  singular values and vectors, yielding low-rank matrices  $\mathbf{A}$  and  $\mathbf{B}$  as:

$$\mathbf{W}^{\text{pri}} = \underbrace{\mathbf{U}_{[:, :r]}}_{\mathbf{A} \in \mathbb{R}^{d \times r}} \sqrt{\mathbf{S}_{[:, :r]}} \underbrace{\sqrt{\mathbf{S}_{[:, :r]}} \mathbf{V}_{[:, :r]}^\top}_{\mathbf{B} \in \mathbb{R}^{r \times n}} \in \mathbb{R}^{d \times n}. \quad (3)$$

Similarly, the residual component  $\mathbf{W}^{\text{res}}$  is derived from the remaining singular values and vectors:

$$\mathbf{W}^{\text{res}} = \mathbf{U}_{[:, :r]} \mathbf{S}_{[r:, r:]} \mathbf{V}_{[r:, r:]}^\top \in \mathbb{R}^{d \times n}. \quad (4)$$

Based on this reconstruction, we define the principal subspace as the one spanned by the low-rank approximation  $\mathbf{W}^{\text{pri}} = \mathbf{A}\mathbf{B}$ , and perform orthogonal fine-tuning within this subspace, yielding fine-tuned weights  $\mathbf{W} = \mathbf{A}\mathbf{R}\mathbf{B}$ , where  $\mathbf{R} \in \mathbb{R}^{r \times r}$  is an orthogonal matrix. However, we observe that **directly using  $\mathbf{A}$  and  $\mathbf{B}$  from PiSSA [12] with an orthogonal  $\mathbf{R}$  fails to preserve the angular relationships among neurons**, as the angular similarity between corresponding columns of  $\mathbf{W}$  and  $\mathbf{W}^{\text{pri}}$  is notably distorted. To address this, we analyze the underlying mechanism and propose Theorem 4.1, which specifies the additional condition required to preserve pairwise angular similarity. A detailed proof is provided in Appendix A.

**Theorem 4.1** (Column-wise Angle Preservation). *Let  $\mathbf{W}^{\text{pri}} = \mathbf{A}\mathbf{B} \in \mathbb{R}^{d \times n}$  and  $\mathbf{W} = \mathbf{A}\mathbf{R}\mathbf{B} \in \mathbb{R}^{d \times n}$ , where  $\mathbf{A} \in \mathbb{R}^{d \times r}$ ,  $\mathbf{B} \in \mathbb{R}^{r \times n}$ , and  $\mathbf{R} \in \mathbb{R}^{r \times r}$  satisfies  $\mathbf{R}^\top \mathbf{R} = \mathbf{R}\mathbf{R}^\top = \mathbf{I}_r$ . Assume  $\text{rank}(\mathbf{A}) = \text{rank}(\mathbf{B}) = r$ , and define  $\mathbf{G} := \mathbf{A}^\top \mathbf{A} \in \mathbb{R}^{r \times r}$ ,  $\mathbf{w}_i^{\text{pri}} := \mathbf{A}\mathbf{b}_i$ , and  $\mathbf{w}_i := \mathbf{A}\mathbf{R}\mathbf{b}_i$  for  $i = 1, \dots, n$ , where  $\mathbf{b}_i$  denotes the  $i$ -th column of  $\mathbf{B}$ . Let  $\theta_{ij}$  (resp.  $\theta_{ij}^{\text{pri}}$ ) denote the angle between  $\mathbf{w}_i$  and  $\mathbf{w}_j$  (resp.  $\mathbf{w}_i^{\text{pri}}$  and  $\mathbf{w}_j^{\text{pri}}$ ). If there exists at least one pair  $i \neq j$  such that  $\mathbf{b}_i^\top \mathbf{G} \mathbf{b}_j \neq 0$ , then*

$$\mathbf{R}^\top \mathbf{G} \mathbf{R} = \mathbf{G} \iff \left( \forall i \neq j, \quad \theta_{ij} = \theta_{ij}^{\text{pri}} \right). \quad (5)$$

Building on the above, we formally propose **Memory-efficient Orthogonal Fine-Tuning (MOFT)** with principal subspace adaptation. MOFT constrains orthogonal fine-tuning to the principal subspace defined by the top- $r$  singular values and vectors from SVD. To preserve hyperspherical energy, it enforces an additional constraint  $\mathbf{A}^\top \mathbf{A} = \mathbf{I}_r$  on the subspace construction. As shown in the right panel of Figure 1a, MOFT freezes the transformed weights and inserts a tunable orthogonal matrix  $\mathbf{R}$  between them. The complete procedure is summarized in Algorithm 1.

Specifically, MOFT performs a one-time SVD on the pre-trained weights before fine-tuning, requiring only a few seconds using fast SVD techniques at negligible cost [33, 12]. To preserve pairwise angular similarity as required by Eq. 5, the principal component  $\mathbf{W}^{\text{pri}}$  in Eq. 3 is reparameterized as:

$$\mathbf{W}^{\text{pri}} = \underbrace{\mathbf{U}_{[:, :r]}}_{\mathbf{A} \in \mathbb{R}^{d \times r}} \underbrace{\mathbf{S}_{[:, :r]} \mathbf{V}_{[:, :r]}^\top}_{\mathbf{B} \in \mathbb{R}^{r \times n}}, \quad (6)$$

where  $\mathbf{A}$  is orthogonal and  $\mathbf{B}$  contains the top- $r$  principal components from SVD. This form ensures that the condition  $\mathbf{R}^\top \mathbf{A}^\top \mathbf{A} \mathbf{R} = \mathbf{A}^\top \mathbf{A}$  holds, preserving angular relationships. The residual  $\mathbf{W}^{\text{res}}$  remains as in Eq. 4, and the forward computation becomes:

$$\mathbf{h} = (\mathbf{W}^{\text{pri}} + \mathbf{W}^{\text{res}})^\top \mathbf{x} = (\mathbf{A}\mathbf{R}\mathbf{B} + \mathbf{W}^{\text{res}})^\top \mathbf{x}, \quad (7)$$

where  $\mathbf{A}$ ,  $\mathbf{B}$ , and  $\mathbf{W}^{\text{res}}$  are frozen, and only the compact orthogonal matrix  $\mathbf{R} \in \mathbb{R}^{r \times r}$  is learnable. The gradient of  $\mathbf{R}$  is computed as  $\frac{\partial L}{\partial \mathbf{R}} = \mathbf{A}^\top \mathbf{x} \left( \frac{\partial L}{\partial \mathbf{h}} \mathbf{B}^\top \right)$ . To ensure that fine-tuning builds upon  $\mathbf{W}^{\text{pre}}$ ,  $\mathbf{R}$  is initialized as the  $r$ -dimensional identity matrix at the start of training.

---

**Algorithm 1** Memory-efficient Orthogonal Fine-Tuning (MOFT)

---

```
1: Input: Pre-trained weight matrix  $\mathbf{W}_{\text{pre}} \in \mathbb{R}^{d \times n}$ , rank  $r$ , input  $x$ , and number of epochs  $E$ 
2: Output: Fine-tuned orthogonal matrix  $\mathbf{R}$  and final weight matrix  $\mathbf{W}_{\text{final}}$ 
3: Initialize: Orthogonal matrix  $\mathbf{R} \leftarrow \mathbf{I}_r$ 
4: Pre-compute:
5:    $\mathbf{W}_{\text{pre}} = \mathbf{U}\mathbf{S}\mathbf{V}^\top$ ,  $\mathbf{A} \leftarrow \mathbf{U}_{[:,r]}$ ,  $\mathbf{B} \leftarrow \mathbf{S}_{[r:,r]} \mathbf{V}_{[:,r]}^\top$ ,  $\mathbf{W}_{\text{res}} \leftarrow \mathbf{U}_{[:,r]} \mathbf{S}_{[r:,r]} \mathbf{V}_{[:,r]}^\top$ 
6: for epoch = 1 to  $E$  do
7:   for each mini-batch  $x$  do
8:      $\mathbf{h} = (\mathbf{A}\mathbf{R}\mathbf{B} + \mathbf{W}_{\text{res}})^\top x$ ,
9:      $\frac{\partial \mathcal{L}}{\partial \mathbf{R}} \leftarrow \mathbf{A}^\top x \left( \frac{\partial \mathcal{L}}{\partial \mathbf{h}} \mathbf{B}^\top \right)$ 
10:     $\mathbf{R} \leftarrow \mathbf{R} - \eta \cdot \frac{\partial \mathcal{L}}{\partial \mathbf{R}}$ 
11:   end for
12: end for
13: Reconstruct:  $\mathbf{W}_{\text{final}} \leftarrow \mathbf{A}\mathbf{R}\mathbf{B} + \mathbf{W}_{\text{res}}$ 
```

---

**Convergence and Stability.** By restricting updates to the principal subspace, MOFT reduces stochastic noise by avoiding perturbations in insignificant directions. This reduction in gradient variance mitigates oscillations and enhances numerical stability during orthogonal fine-tuning. Although the theoretical convergence rate remains  $O(1/k)$ , the reduced noise enables more stable and efficient adaptation in practice. A detailed analysis is provided in Appendix B.

**Connection to Orthogonal Fine-Tuning.** MOFT can be viewed as a memory- and computation-efficient special case of full-space orthogonal fine-tuning, represented as:

$$\mathbf{R}_{\text{full}} = \begin{pmatrix} \mathbf{R} & 0 \\ 0 & \mathbf{I}_{(d-r)} \end{pmatrix}, \quad (8)$$

where  $\mathbf{R}$  is an orthogonal transformation applied to the principal subspace  $\mathbf{W}^{\text{pr}}$ , and  $\mathbf{I}_{(d-r)}$  denotes the identity on the residual subspace  $\mathbf{W}^{\text{res}}$ . A complete proof is provided in Appendix C.

**Memory-Efficient Fine-Tuning.** MOFT reduces activation memory by lowering the dimensionality of trainable matrices from  $O(d)$  to  $O(r)$ . Building on prior analysis [34], we examine activation memory usage across PEFT methods (see Appendix D), showing that it primarily depends on the fine-tuning structure, the size of each trainable matrix, and their total number. BOFT and GOFT incur substantially higher overhead due to storing activations for multiple full-dimensional sparse matrices. In contrast, MOFT mitigates this cost by operating directly in a reduced subspace.

**Cayley Parameterization.** Following prior work [11, 13], we adopt the Cayley parameterization [35] to enforce the orthogonality of  $\mathbf{R}$ , where  $\mathbf{R} = (\mathbf{I} - \mathbf{Q})(\mathbf{I} + \mathbf{Q})^{-1}$  and  $\mathbf{Q} = -\mathbf{Q}^\top$  is a skew-symmetric matrix. When  $(\mathbf{I} + \mathbf{Q})$  is non-invertible, a pseudo-inverse is applied. This parameterization reduces the number of trainable parameters from  $r^2$  to  $r(r-1)/2$ , yielding nearly 50% compression. While it limits representational flexibility, it also serves as an explicit regularizer during fine-tuning [11, 13]. Importantly,  $\mathbf{R}$  can be merged into the weight matrix without incurring additional inference latency. Further details are provided in Appendix E.

**Number of Trainable Parameters.** We compare trainable parameter counts across PEFT methods in Appendix F. Unlike most approaches, MOFT decouples parameter count from hidden dimension, maintaining a constant size determined solely by rank  $r$ . This design supports scalability and allows a single pre-trained model to host multiple task-specific  $\Delta \mathbf{R}$  matrices for efficient multi-task adaptation. As MOFT tunes only a compact  $r \times r$  matrix, it enables efficient and fast deployment. To match LoRA’s performance at  $r = 8$ , MOFT typically requires a higher rank ( $6 \sim 24 \times$ ). A larger  $r$  improves accuracy toward full-space orthogonal fine-tuning but comes with increased parameter overhead.

**Relaxation of Orthogonality Constraints.** Empirical evidence suggests that relaxing strict orthogonality—both in pairwise angular similarity and neuron magnitudes—can improve adaptation [11, 13, 14]. To increase flexibility across diverse tasks, we extend MOFT by introducing two learnable scaling vectors that modulate input and output magnitudes before and after the orthogonal

Table 1: Experimental results using LLaMA-3.1-8B [1] on eight commonsense reasoning benchmarks. The best and second-best results for each dataset are marked in **bold** and underline (except FFT), respectively. Accuracy (%) is reported for all sub-datasets.

Methods	#Params	Inserted Modules	Mem (GB)	BoolQ	PIQA	SIQA	HS	WG	ARC-e	ARC-c	OBQA	Avg.
FFT	8B	-	74.88	72.02	85.91	72.98	90.15	71.98	91.58	81.89	81.60	81.02
LoRA <sub>r=1</sub>	1.77M	Q,K,V,U,D	53.93	71.13	<u>85.31</u>	<b>74.67</b>	89.08	<u>72.61</u>	90.24	78.16	<u>82.40</u>	80.45
PiSSA <sub>r=1</sub>	1.77M	Q,K,V,U,D	53.93	<b>72.05</b>	84.60	74.21	89.93	70.88	90.15	79.01	82.00	80.35
DoRA <sub>r=1</sub>	2.56M	Q,K,V,U,D	65.40	71.05	85.29	73.25	<u>90.09</u>	<b>73.32</b>	<u>90.74</u>	<u>79.75</u>	81.87	<u>80.67</u>
BOFT <sub>m=2</sub> <sup>b=2</sup>	1.12M	Q,V	79.38	69.66	83.95	71.65	80.87	70.01	90.40	77.82	79.00	77.92
LoRA <sub>r=1</sub>	0.59M	Q,K,V	52.78	66.97	83.08	71.03	77.06	64.01	90.70	77.39	78.80	76.13
SVFT <sub>P</sub>	0.46M	Q,K,V,U,D	65.82	65.08	81.07	69.40	85.69	68.82	88.47	77.05	76.00	76.45
LoRA-XS <sub>r=48</sub>	0.37M	Q,K,V,U,D	53.40	69.30	84.82	71.29	87.44	67.01	89.39	77.22	82.60	78.63
MOFT <sub>r=72</sub>	0.43M	Q,K,V,U,D	53.70	69.72	84.39	72.01	87.99	68.67	90.19	78.16	81.00	79.02
MOFT <sub>r=184</sub>	2.75M	Q,K,V,U,D	55.02	<u>71.65</u>	<b>86.07</b>	<u>74.26</u>	<b>90.84</b>	72.45	<b>90.95</b>	<b>79.95</b>	<b>83.60</b>	<b>81.22</b>

transformation. The resulting forward computation is:

$$\mathbf{h} = (\mathbf{A} \text{diag}(\boldsymbol{\alpha}) \mathbf{R} \text{diag}(\boldsymbol{\beta}) \mathbf{B} + \mathbf{W}^{\text{res}})^{\top} \mathbf{x}, \quad (9)$$

where  $\boldsymbol{\alpha}$  and  $\boldsymbol{\beta}$  are initialized as all-one vectors to preserve the pre-trained weights. During training, both angular and magnitude properties of  $\mathbf{W}$  adapt to task-specific objectives. Orthogonality in both aspects is relaxed once  $\text{diag}(\boldsymbol{\alpha})$  or  $\text{diag}(\boldsymbol{\beta})$  deviates from a scalar identity matrix  $\lambda \mathbf{I}$ . Angular relationships are preserved and magnitudes uniformly scaled only when  $\text{diag}(\boldsymbol{\alpha}) = \lambda_1 \mathbf{I}$  and  $\text{diag}(\boldsymbol{\beta}) = \lambda_2 \mathbf{I}$ . All main results are obtained using MOFT with both scaling vectors enabled.

## 5 Experiments

To evaluate MOFT, we conduct experiments on 37 tasks spanning language and vision domains. We use encoder-only models (DeBERTaV3-base [17], ViT-B/16 [2]) and decoder-only models (LLaMA-3.2-3B [18], LLaMA-3.1-8B [1]). These models are fine-tuned on tasks including commonsense reasoning [36, Commonsense-15K], mathematical QA [37, MetaMathQA-40K], natural language understanding [15, GLUE], and visual classification [16, VTAB-1K]. All experiments are run on a single RTX 4090 (24GB) or H100-SXM (80GB) GPU.

**Baselines.** We employ full fine-tuning and state-of-the-art PEFT methods as baselines for comparison:

- **FFT** [38] updates all model weights during the fine-tuning process.
- **LoRA** [9] keeps the pre-trained weights frozen and adjusts only two low-rank matrices.
- **PiSSA** [12] improves the initialization of LoRA to fine-tune only the principal weights.
- **DoRA** [10] separates the adaptation into two components including direction and magnitude.
- **BOFT** [13] replaces large orthogonal operations with sparse matrix multiplications.
- **SVFT** [27] perturbs the primary diagonal and off-diagonals of the singular value matrix.
- **LoRA-XS** [29] injects a single learnable matrix between the low-rank matrices of LoRA.

### 5.1 Commonsense Reasoning

**Experimental Setup.** Following prior work [36, 10, 27], we fine-tune LLaMA-3.1-8B [1] on the Commonsense-15K dataset [36]. Due to memory constraints, BOFT is applied only to the  $Q$  and  $V$  modules, whereas other baselines are applied to all  $Q, K, V, U, D$  modules. We include LoRA<sub>r=1</sub>, applied to the  $Q, K, V$  modules, to ensure parameter efficiency comparable to other baselines. All experiments use the FP32 data type for fine-tuning, except FFT, which adopts BF16 [39] to reduce computational overhead. We adopt a gradient accumulation strategy with small batch sizes ( $\leq 4$ ) to approximate large-batch training. Appendix G details the hyperparameter settings.

Table 2: Experimental results using LLaMA-3.2-3B [18] on GSM-8K [40] and MATH [41]. The best and second-best results for each dataset are marked in **bold** and underline (except FFT), respectively. Accuracy (%) is reported for both GSM-8K and MATH datasets.

Methods	#Params	Inserted Modules	Mem (GB)	GSM-8K	MATH
FFT	3B	-	37.35	63.00	16.84
LoRA <sub>r=1</sub>	1.52M	Q,K,V,U,D,O,G	32.02	57.32	12.88
PiSSA <sub>r=1</sub>	1.52M	Q,K,V,U,D,O,G	32.02	56.48	13.18
DoRA <sub>r=1</sub>	2.29M	Q,K,V,U,D,O,G	43.17	<u>57.54</u>	<u>13.60</u>
BOFT <sub>m=2</sub> <sup>b=2</sup>	1.18M	Q,K,V	48.16	52.46	10.78
LoRA <sub>r=1</sub>	0.40M	Q,K,V	30.14	47.23	10.36
SVFT <sub>P</sub>	0.49M	Q,K,V,U,D,O,G	41.07	52.01	12.18
LoRA-XS <sub>r=48</sub>	0.45M	Q,K,V,U,D,O,G	32.34	51.86	9.80
MOFT <sub>r=72</sub>	0.53M	Q,K,V,U,D,O,G	32.66	52.01	12.44
MOFT <sub>r=152</sub>	2.31M	Q,K,V,U,D,O,G	33.50	<b>58.23</b>	<b>13.66</b>

**Results.** As illustrated in Table 1, MOFT outperforms key baselines in average performance while significantly reducing peak memory usage for orthogonal fine-tuning. Under extremely low parameter budgets ( $\leq 1\text{M}$ ), MOFT<sub>r=72</sub> improves average performance by 2.89% over LoRA and 1.10% over BOFT, with 32.73% lower peak memory than BOFT. With more trainable parameters, MOFT<sub>r=184</sub> achieves the best or second-best results on 7 of 8 sub-datasets, outperforming FFT on average, surpassing DoRA by 0.55%, and reducing peak memory usage by 15.87%. Due to small actual batch sizes, the memory advantage of MOFT over LoRA appears less pronounced in this setting.

## 5.2 Mathematical Question Answering

**Experimental Setup.** Following [13, 27], we fine-tune models on MetaMathQA-40K [37] and evaluate performance on GSM-8K [40] and MATH [41] using the LLaMA-3.2-3B [18] model. To prevent out-of-memory issues, BOFT is applied only to the  $Q, K, V$  modules, while other PEFT baselines are applied to all linear layers. LoRA<sub>r=1</sub> is also restricted to the  $Q, K, V$  modules for a fair comparison. Bit-width settings follow those in Section 5.1, and all methods use gradient accumulation. Additional hyperparameter details are provided in Appendix H.

**Results.** As shown in Table 2, MOFT outperforms all baselines on both GSM-8K and MATH, while offering improved memory efficiency. On MATH, MOFT<sub>r=72</sub> improves accuracy by 2.64%, 2.08%, and 1.66% over LoRA-XS, LoRA, and BOFT, respectively, and reduces peak memory by up to 32.18% compared to BOFT. Against DoRA, MOFT<sub>r=152</sub> achieves comparable or better performance with 22.40% lower memory usage. Notably, PiSSA<sub>r=1</sub> underperforms DoRA<sub>r=1</sub>, highlighting the limitations of principal component-based tuning under extreme parameter constraints. In contrast, MOFT alleviates this issue by performing orthogonal fine-tuning within the principal subspace, achieving strong performance and memory efficiency. While a performance gap remains between PEFT and FFT on complex reasoning tasks, MOFT substantially narrows this gap as the parameter budget increases. Due to memory constraints, gradient accumulation is required, resulting in small effective batch sizes that make MOFT’s memory usage comparable to LoRA.

## 5.3 Natural Language Understanding

**Experimental Setup.** We evaluate MOFT by fine-tuning the DeBERTaV3-base [17] model on the GLUE benchmark [15]. As the model does not encounter memory bottlenecks, all PEFT methods are applied to every linear layer without gradient accumulation. To reduce redundancy and computational cost on large datasets such as MNLI, QQP, and QNLI, we adopt results from prior work [27] and follow the same experimental setup. As prior works rarely report peak memory usage on GLUE, we additionally measure the peak memory consumption of various PEFT methods on the CoLA datasets. Further details on datasets and training configurations are provided in Appendix I.

**Results.** As illustrated in Table 3, MOFT achieves the highest average performance on the GLUE benchmark while substantially reducing the memory overhead of orthogonal fine-tuning—surpassing

Table 3: Experimental results fine-tuned using DeBERTaV3-base [17] on the GLUE validation set. The best and second-best results for each dataset are marked in **bold** and underline (except FFT), respectively. We report the mean results of 5 runs from different random seeds. \* indicates numbers published in prior work [27, 14].

Methods	#Params	MNLI	SST-2	MRPC	CoLA	QNLI	QQP	RTE	STS-B	Avg.
*FFT	184M	89.90	95.63	89.46	69.19	94.03	92.40	83.75	91.60	88.25
*LoRA <sub>r=8</sub>	1.33M	<b>90.65</b>	94.95	89.95	69.82	93.87	<b>91.99</b>	85.20	91.60	88.50
*DoRA <sub>r=4</sub>	0.75M	89.92	95.41	89.10	69.37	94.14	<u>91.53</u>	<u>87.00</u>	<b>91.80</b>	88.53
*OFT <sub>b=4</sub>	0.33M	89.20	95.18	89.46	<u>70.82</u>	93.04	<u>90.27</u>	83.39	91.01	87.80
*LoRA <sub>r=1</sub>	0.17M	90.12	95.64	86.43	69.13	<u>94.18</u>	91.43	<b>87.36</b>	91.52	88.23
*GOFT	0.08M	90.01	<u>96.10</u>	90.44	<b>71.64</b>	<u>93.52</u>	90.85	86.28	91.42	<u>88.78</u>
*SVFT <sub>P</sub>	0.06M	89.69	95.41	88.77	70.95	<b>94.27</b>	90.16	87.24	<b>91.80</b>	88.54
LoRA-XS <sub>r=32</sub>	0.07M	89.55	95.38	89.81	69.42	93.72	90.02	85.78	<u>91.73</u>	88.18
MOFT <sub>r=48</sub>	0.09M	89.62	95.62	<u>91.08</u>	70.69	93.78	90.27	86.07	91.63	88.60
MOFT <sub>r=144</sub>	0.76M	<u>90.38</u>	<b>96.19</b>	<b>91.32</b>	70.53	94.06	91.51	86.50	91.66	<b>89.02</b>

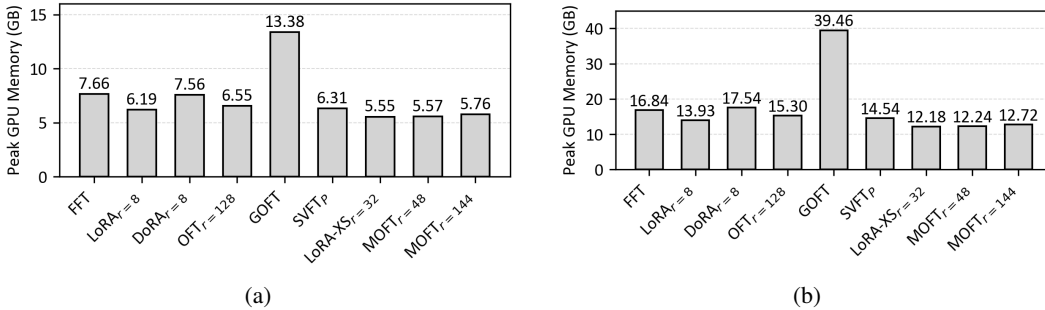


Figure 2: Comparison of peak memory usage across different PEFT methods on the CoLA dataset with (a) DeBERTaV3-base and (b) DeBERTaV3-large [17] (maximum sequence lengths is 64).

even LoRA in memory efficiency. MOFT<sub>r=48</sub> matches the average performance of GOFT while reducing peak memory by 2.3 ~ 3.1×, as shown in Figure 2. With increased parameter budgets, MOFT<sub>r=144</sub> outperforms key baselines such as DoRA and LoRA, incurring only minimal memory overhead. Since MOFT reduces overall memory usage by lowering activation storage, larger batch sizes further amplify its advantage over LoRA. Although LoRA-XS achieves low memory usage, its performance remains significantly lower than that of MOFT. These results highlight that MOFT offers a favorable trade-off between performance and memory efficiency in PEFT.

## 5.4 Visual Classification

**Experimental Setup.** Beyond NLP, we evaluate MOFT on vision tasks by fine-tuning ViT-B/16 [2] on the VTAB-1K benchmark [16], which covers 19 diverse visual classification datasets. Following [13, 14], all methods are applied to every linear layer in the backbone and trained with batch size 64 without gradient accumulation. To ensure a fair comparison, all baselines are implemented within a unified framework built on HuggingFace’s PEFT and Transformers libraries. We introduce specialized vision PEFT methods such as FacT [42]. Further details are provided in Appendix J.

**Results.** As shown in Table 4, MOFT achieves the highest average performance across vision tasks while incurring the lowest peak memory among all baselines. MOFT<sub>r=184</sub> outperforms BOFT and DoRA by 3.3% and 2.1%, using only 38.20% and 56.88% of their memory, respectively. MOFT<sub>r=48</sub> and LoRA-XS<sub>r=32</sub> achieve the lowest memory usage, with MOFT performing 1.5% better on average. Figure 1b further shows that MOFT consistently consumes less memory than BOFT across all batch sizes, and its advantage over FFT and LoRA becomes more pronounced as batch size increases. MOFT matches the average performance of the specialized vision PEFT methods FacT while using 27% less memory. These results highlight the effectiveness and efficiency of MOFT in vision tasks.

Table 4: Experimental results using ViT-B/16 on the VTAB-1K benchmark. Top-1 accuracy (%) is reported for all sub-datasets. We report the mean results of 5 runs from different random seeds.

Methods	Mem (GB)	Natural						Specialized				Structured						Avg			
		Cifar100	Caltech101	DTD102	Flower102	Pets	SVHN	Sun397	Camelyon	EuroSAT	Resisc45	Retinopathy	Clevr-Count	Clevr-Dist	DMLab	KITTI-Dist	dSpr-Loc		dSpr-Ori	sNORB-Azim	sNORB-Ele
FFT	8.2	70.7	89.3	69.5	99.0	90.4	81.7	54.9	85.4	93.6	83.8	74.5	58.3	51.5	43.2	75.0	73.1	48.7	16.4	30.0	67.8
LoRA <sub>r=8</sub>	9.9	71.4	88.4	70.1	99.0	91.4	76.6	55.7	85.9	94.2	83.3	74.1	72.0	54.3	43.0	76.6	74.8	48.6	16.4	31.8	68.8
DoRA <sub>r=8</sub>	17.8	71.4	88.4	70.6	98.9	91.4	76.4	55.6	84.3	94.2	83.4	74.2	71.8	54.0	43.8	76.0	76.3	47.6	16.2	31.4	68.7
BOFT <sub>m=2</sub> <sup>b=2</sup>	10.9	66.5	88.6	68.0	98.7	89.9	84.9	53.8	85.3	94.1	82.1	74.3	59.3	53.1	44.6	75.4	79.2	49.1	16.5	30.4	67.5
SVFT <sub>P</sub>	7.9	68.6	87.6	68.8	98.9	91.1	71.3	54.5	84.2	93.8	80.3	74.5	58.6	49.0	40.7	74.3	70.0	46.6	14.9	29.9	66.2
LoRA-XS <sub>r=32</sub>	6.2	65.4	89.2	67.9	98.9	88.8	84.9	53.8	82.9	94.1	80.8	73.7	61.9	57.0	44.9	78.1	80.2	48.3	17.3	31.4	68.4
Fact-TT <sub>r=16</sub>	9.1	73.2	86.7	71.3	99.0	91.4	84.3	55.4	86.2	95.0	85.0	71.6	78.2	58.8	46.8	75.1	79.5	50.9	16.4	35.2	70.5
Fact-TK <sub>r=32</sub>	9.3	73.5	87.1	70.6	98.9	91.8	85.0	55.2	84.8	95.4	85.4	71.3	78.2	58.4	47.5	75.8	80.4	51.6	16.2	36.8	70.7
MOFT <sub>r=48</sub>	6.2	70.9	88.2	69.4	98.9	91.6	86.0	55.3	83.3	93.7	81.9	74.6	71.4	58.9	44.7	78.0	78.8	51.4	20.1	31.7	69.9
MOFT <sub>r=184</sub>	6.8	71.5	89.4	69.5	99.1	91.8	88.3	54.9	84.7	93.6	83.2	74.8	69.6	59.7	46.5	79.3	82.4	53.6	20.5	33.5	70.8

Table 5: Effect of initialization on RTE and CoLA [15] with the DeBERTaV3-base [17] model.

Method ( $r = 64$ )	RTE (%)	CoLA (%)
$A_{orth}R_{orth}B$ (MOFT)	85.92	70.63
$AR_{orth}B_{orth}$	52.71	67.97
$AR_{orth}B$	71.11	69.23
$A_{orth}RB$	85.56	69.24

## 5.5 Ablation Studies

**Effect of Initialization.** We assess the impact of different initialization strategies for MOFT by comparing four variants:  $A_{orth}R_{orth}B$ ,  $AR_{orth}B_{orth}$ ,  $AR_{orth}B$ , and  $A_{orth}RB$ , where  $A$  and  $B$  are initialized using PiSSA [12], and  $A_{orth}$  denotes orthogonal initialization of matrix  $A$ . As shown in Table 5, the initialization  $A_{orth}R_{orth}B$  (i.e., MOFT) achieves the best performance, highlighting the importance of preserving pairwise angular similarity between neurons.

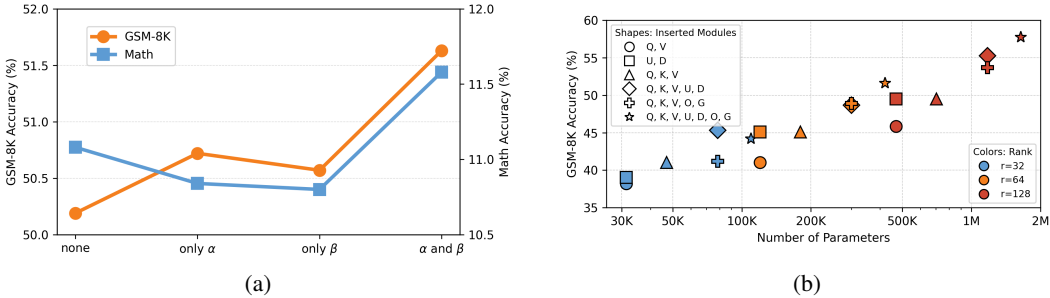


Figure 3: (a) Effect of scaling vectors on GSM-8K and MATH using LLaMA-3.2-3B with  $r = 64$ . (b) Effect of inserted modules on GSM-8K using LLaMA-3.2-3B.

**Effect of Scaling Vectors  $\alpha$  and  $\beta$ .** We evaluate the role of scaling vectors on GSM-8K and MATH, with MOFT applied to all linear layers. As shown in Figure 3a, using both  $\alpha$  and  $\beta$  leads to consistently better performance across tasks. We hypothesize that single-sided scaling lacks sufficient capacity to capture task-specific variations, resulting in sub-optimal adaptation.

**Effect of Inserted Modules.** We test MOFT on GSM-8K under different insertion schemes, and the results are illustrated in Figure 3b. With fixed rank  $r$ , applying MOFT to the  $Q, K, V, U, D$  modules typically yields the best trade-off between performance and parameter efficiency. When the parameter budget permits, inserting MOFT into all linear layers generally provides the best overall results.

## 6 Conclusion

In this work, we present MOFT, a novel PEFT framework that confines orthogonal fine-tuning to the principal subspace and improves adaptability through two learnable scaling vectors. Extensive experiments validate its strong performance and memory efficiency. MOFT represents a promising direction for scalable and efficient fine-tuning, particularly in resource-constrained settings.

## References

- [1] A. Dubey, A. Jauhri, A. Pandey, A. Kadian, A. Al-Dahle, A. Letman, A. Mathur, A. Schelten, A. Yang, A. Fan *et al.*, “The llama 3 herd of models,” *arXiv preprint arXiv:2407.21783*, 2024.
- [2] A. Dosovitskiy, L. Beyer, A. Kolesnikov, D. Weissenborn, X. Zhai, T. Unterthiner, M. Dehghani, M. Minderer, G. Heigold, S. Gelly, J. Uszkoreit, and N. Houlsby, “An image is worth 16x16 words: Transformers for image recognition at scale,” in *The Ninth International Conference on Learning Representations*, 2021.
- [3] C. Qin, A. Zhang, Z. Zhang, J. Chen, M. Yasunaga, and D. Yang, “Is chatGPT a general-purpose natural language processing task solver?” in *The 2023 Conference on Empirical Methods in Natural Language Processing*, 2023.
- [4] H. Liu, C. Li, Q. Wu, and Y. J. Lee, “Visual instruction tuning,” in *Thirty-seventh Conference on Neural Information Processing Systems*, 2023.
- [5] J. Wei, Y. Tay, R. Bommasani, C. Raffel, B. Zoph, S. Borgeaud, D. Yogatama, M. Bosma, D. Zhou, D. Metzler, E. H. Chi, T. Hashimoto, O. Vinyals, P. Liang, J. Dean, and W. Fedus, “Emergent abilities of large language models,” *Transactions on Machine Learning Research*, 2022.
- [6] B. Lester, R. Al-Rfou, and N. Constant, “The power of scale for parameter-efficient prompt tuning,” in *Proceedings of the 2021 Conference on Empirical Methods in Natural Language Processing*, 2021, pp. 3045–3059.
- [7] X. L. Li and P. Liang, “Prefix-tuning: Optimizing continuous prompts for generation,” in *Proceedings of the 59th Annual Meeting of the Association for Computational Linguistics and the 11th International Joint Conference on Natural Language Processing (Volume 1: Long Papers)*, 2021, pp. 4582–4597.
- [8] N. Houlsby, A. Giurgiu, S. Jastrzebski, B. Morrone, Q. De Laroussilhe, A. Gesmundo, M. Attariyan, and S. Gelly, “Parameter-efficient transfer learning for nlp,” in *International Conference on Machine Learning*, 2019, pp. 2790–2799.
- [9] E. J. Hu, Y. Shen, P. Wallis, Z. Allen-Zhu, Y. Li, S. Wang, L. Wang, and W. Chen, “Lora: Low-rank adaptation of large language models,” *arXiv preprint arXiv:2106.09685*, 2021.
- [10] S.-Y. Liu, C.-Y. Wang, H. Yin, P. Molchanov, Y.-C. F. Wang, K.-T. Cheng, and M.-H. Chen, “Dora: Weight-decomposed low-rank adaptation,” in *International Conference on Machine Learning*, 2024.
- [11] Z. Qiu, W. Liu, H. Feng, Y. Xue, Y. Feng, Z. Liu, D. Zhang, A. Weller, and B. Schölkopf, “Controlling text-to-image diffusion by orthogonal finetuning,” *Advances in Neural Information Processing Systems*, vol. 36, pp. 79 320–79 362, 2023.
- [12] F. Meng, Z. Wang, and M. Zhang, “PiSSA: Principal singular values and singular vectors adaptation of large language models,” in *The Thirty-eighth Annual Conference on Neural Information Processing Systems*, 2024.
- [13] W. Liu, Z. Qiu, Y. Feng, Y. Xiu, Y. Xue, L. Yu, H. Feng, Z. Liu, J. Heo, S. Peng, Y. Wen, M. J. Black, A. Weller, and B. Schölkopf, “Parameter-efficient orthogonal finetuning via butterfly factorization,” in *The Twelfth International Conference on Learning Representations*, 2024.
- [14] X. Ma, X. Chu, Z. Yang, Y. Lin, X. Gao, and J. Zhao, “Parameter efficient quasi-orthogonal fine-tuning via givens rotation,” in *International Conference on Machine Learning*, 2024.
- [15] A. Wang, “Glue: A multi-task benchmark and analysis platform for natural language understanding,” *arXiv preprint arXiv:1804.07461*, 2018.
- [16] X. Zhai, J. Puigcerver, A. Kolesnikov, P. Ruysen, C. Riquelme, M. Lucic, J. Djolonga, A. S. Pinto, M. Neumann, A. Dosovitskiy *et al.*, “A large-scale study of representation learning with the visual task adaptation benchmark,” *arXiv preprint arXiv:1910.04867*, 2019.

- [17] P. He, J. Gao, and W. Chen, “Debertav3: Improving deberta using electra-style pre-training with gradient-disentangled embedding sharing,” *arXiv preprint arXiv:2111.09543*, 2021.
- [18] Meta AI, “Llama 3.2: Revolutionizing edge ai and vision with open, customizable models,” <https://ai.meta.com/blog/llama-3-2-connect-2024-vision-edge-mobile-devices/>, September 2024.
- [19] C. Li, H. Farkhoor, R. Liu, and J. Yosinski, “Measuring the intrinsic dimension of objective landscapes,” in *The Sixth International Conference on Learning Representations*, 2018.
- [20] A. Aghajanyan, S. Gupta, and L. Zettlemoyer, “Intrinsic dimensionality explains the effectiveness of language model fine-tuning,” in *Proceedings of the 59th Annual Meeting of the Association for Computational Linguistics and the 11th International Joint Conference on Natural Language Processing (Volume 1: Long Papers)*, 2021, pp. 7319–7328.
- [21] E. B. Zaken, Y. Goldberg, and S. Ravfogel, “BitFit: Simple parameter-efficient fine-tuning for transformer-based masked language-models,” in *Proceedings of the 60th Annual Meeting of the Association for Computational Linguistics (Volume 2: Short Papers)*, 2022, pp. 1–9.
- [22] W. Song, Z. Li, L. Zhang, hai zhao, and B. Du, “Sparse is enough in fine-tuning pre-trained large language models,” in *Forty-first International Conference on Machine Learning*, 2024.
- [23] J. Xu and J. Zhang, “Random masking finds winning tickets for parameter efficient fine-tuning,” in *International Conference on Machine Learning*, 2024.
- [24] J. Pfeiffer, A. Kamath, A. Rücklé, K. Cho, and I. Gurevych, “Adapterfusion: Non-destructive task composition for transfer learning,” *arXiv preprint arXiv:2005.00247*, 2020.
- [25] X. Liu, K. Ji, Y. Fu, W. Tam, Z. Du, Z. Yang, and J. Tang, “P-tuning: Prompt tuning can be comparable to fine-tuning across scales and tasks,” in *Proceedings of the 60th Annual Meeting of the Association for Computational Linguistics (Volume 2: Short Papers)*, 2022, pp. 61–68.
- [26] D. J. Kopiczko, T. Blankevoort, and Y. M. Asano, “VeRA: Vector-based random matrix adaptation,” in *The Twelfth International Conference on Learning Representations*, 2024.
- [27] V. Lingam, A. T. Neerkaje, A. Vavre, A. Shetty, G. K. Gudur, J. Ghosh, E. Choi, A. Dimakis, A. Bojchevski, and sujay sanghavi, “SVFT: Parameter-efficient fine-tuning with singular vectors,” in *The Thirty-eighth Annual Conference on Neural Information Processing Systems*, 2024.
- [28] Z. Gao, Q. Wang, A. Chen, Z. Liu, B. Wu, L. Chen, and J. Li, “Parameter-efficient fine-tuning with discrete fourier transform,” in *International Conference on Machine Learning*, 2024.
- [29] K. Bałazy, M. Banaei, K. Aberer, and J. Tabor, “Lora-xs: Low-rank adaptation with extremely small number of parameters,” *arXiv preprint arXiv:2405.17604*, 2024.
- [30] W. Liu, R. Lin, Z. Liu, J. M. Rehg, L. Paull, L. Xiong, L. Song, and A. Weller, “Orthogonal over-parameterized training,” in *Proceedings of the IEEE/CVF Conference on Computer Vision and Pattern Recognition*, 2021, pp. 7251–7260.
- [31] F. Zhang and M. Pilanci, “Spectral adapter: Fine-tuning in spectral space,” in *The Thirty-eighth Annual Conference on Neural Information Processing Systems*, 2024.
- [32] S. Azizi, S. Kundu, and M. Pedram, “LaMDA: Large model fine-tuning via spectrally decomposed low-dimensional adaptation,” in *Findings of the Association for Computational Linguistics: EMNLP 2024*, 2024, pp. 9635–9646.
- [33] N. Halko, P.-G. Martinsson, and J. A. Tropp, “Finding structure with randomness: Probabilistic algorithms for constructing approximate matrix decompositions,” *SIAM review*, vol. 53, no. 2, pp. 217–288, 2011.
- [34] V. A. Korthikanti, J. Casper, S. Lym, L. McAfee, M. Andersch, M. Shoeybi, and B. Catanzaro, “Reducing activation recomputation in large transformer models,” *Proceedings of Machine Learning and Systems*, vol. 5, pp. 341–353, 2023.
- [35] A. Cayley, *The collected mathematical papers of Arthur Cayley*. University of Michigan Library, 1894, vol. 7.
- [36] Z. Hu, L. Wang, Y. Lan, W. Xu, E.-P. Lim, L. Bing, X. Xu, S. Poria, and R. Lee, “LLM-adapters: An adapter family for parameter-efficient fine-tuning of large language models,” in *Proceedings of the 2023 Conference on Empirical Methods in Natural Language Processing*, 2023, pp. 5254–5276.

- [37] L. Yu, W. Jiang, H. Shi, J. YU, Z. Liu, Y. Zhang, J. Kwok, Z. Li, A. Weller, and W. Liu, “Metamath: Bootstrap your own mathematical questions for large language models,” in *The Twelfth International Conference on Learning Representations*, 2024.
- [38] J. Howard and S. Ruder, “Universal language model fine-tuning for text classification,” in *Proceedings of the 56th Annual Meeting of the Association for Computational Linguistics (Volume 1: Long Papers)*, 2018, pp. 328–339.
- [39] S. Wang and P. Kanwar, “Bfloat16: The secret to high performance on cloud tpus,” August 2019, google Cloud Blog. [Online]. Available: <https://cloud.google.com/blog/products/ai-machine-learning/bfloat16-the-secret-to-high-performance-on-cloud-tpus>
- [40] K. Cobbe, V. Kosaraju, M. Bavarian, M. Chen, H. Jun, L. Kaiser, M. Plappert, J. Tworek, J. Hilton, R. Nakano *et al.*, “Training verifiers to solve math word problems,” *arXiv preprint arXiv:2110.14168*, 2021.
- [41] D. Hendrycks, C. Burns, S. Kadavath, A. Arora, S. Basart, E. Tang, D. Song, and J. Steinhardt, “Measuring mathematical problem solving with the MATH dataset,” in *Thirty-fifth Conference on Neural Information Processing Systems Datasets and Benchmarks Track (Round 2)*, 2021.
- [42] S. Jie and Z.-H. Deng, “Fact: Factor-tuning for lightweight adaptation on vision transformer,” in *Proceedings of AAAI Conference on Artificial Intelligence (AAAI)*, 2023.
- [43] H. Karimi, J. Nutini, and M. Schmidt, “Linear convergence of gradient and proximal-gradient methods under the polyak-łojasiewicz condition,” in *Machine Learning and Knowledge Discovery in Databases: European Conference, ECML PKDD 2016, Riva del Garda, Italy, September 19-23, 2016, Proceedings, Part I 16*. Springer, 2016, pp. 795–811.
- [44] S. Mangrulkar, S. Gugger, L. Debut, Y. Belkada, S. Paul, and B. Bossan, “Peft: State-of-the-art parameter-efficient fine-tuning methods,” <https://github.com/huggingface/peft>, 2022.
- [45] C. Clark, K. Lee, M.-W. Chang, T. Kwiatkowski, M. Collins, and K. Toutanova, “BoolQ: Exploring the surprising difficulty of natural yes/no questions,” in *Proceedings of the 2019 Conference of the North American Chapter of the Association for Computational Linguistics: Human Language Technologies, Volume 1 (Long and Short Papers)*, 2019, pp. 2924–2936.
- [46] Y. Bisk, R. Zellers, J. Gao, Y. Choi *et al.*, “Piqa: Reasoning about physical commonsense in natural language,” in *Proceedings of the AAAI conference on artificial intelligence*, vol. 34, 2020, pp. 7432–7439.
- [47] M. Sap, H. Rashkin, D. Chen, R. Le Bras, and Y. Choi, “Social IQa: Commonsense reasoning about social interactions,” in *Proceedings of the 2019 Conference on Empirical Methods in Natural Language Processing and the 9th International Joint Conference on Natural Language Processing (EMNLP-IJCNLP)*, 2019, pp. 4463–4473.
- [48] R. Zellers, A. Holtzman, Y. Bisk, A. Farhadi, and Y. Choi, “Hellaswag: Can a machine really finish your sentence?” *arXiv preprint arXiv:1905.07830*, 2019.
- [49] K. Sakaguchi, R. L. Bras, C. Bhagavatula, and Y. Choi, “Winogrande: An adversarial winograd schema challenge at scale,” *Communications of the ACM*, vol. 64, no. 9, pp. 99–106, 2021.
- [50] P. Clark, I. Cowhey, O. Etzioni, T. Khot, A. Sabharwal, C. Schoenick, and O. Tafjord, “Think you have solved question answering? try arc, the ai2 reasoning challenge,” *arXiv preprint arXiv:1803.05457*, 2018.
- [51] T. Mihaylov, P. Clark, T. Khot, and A. Sabharwal, “Can a suit of armor conduct electricity? a new dataset for open book question answering,” in *Proceedings of the 2018 Conference on Empirical Methods in Natural Language Processing*, 2018, pp. 2381–2391.
- [52] A. Paszke, S. Gross, F. Massa, A. Lerer, J. Bradbury, G. Chanan, T. Killeen, Z. Lin, N. Gimelshein, L. Antiga *et al.*, “Pytorch: An imperative style, high-performance deep learning library,” *Advances in neural information processing systems*, vol. 32, 2019.

## Organization of the Appendix

The appendix is organized as follows:

- Appendix A presents the theoretical proof for the column-wise angle preservation theorem.
- Appendix B analyzes the convergence and stability of MOFT.
- Appendix C proves the connection between MOFT and full-space orthogonal fine-tuning.
- Appendix D reports activation memory statistics for different PEFT methods.
- Appendix E provides theoretical details of the Cayley parameterization.
- Appendix F compares the number of trainable parameters across popular PEFT methods.
- Appendix G describes experimental details for commonsense reasoning on Commonsense-15K.
- Appendix H provides experimental details for mathematical question answering on MetaMathQA-40K.
- Appendix I outlines experimental details for natural language understanding on GLUE.
- Appendix J covers experimental details for visual classification on VTAB-1K.
- Appendix K presents computational cost comparisons of various PEFT methods.
- Appendix L reports extended experiments on the effects of SVD initialization and different rank settings.
- Appendix M provides standard deviations on GLUE and VTAB-1K benchmarks.

## A Proof for the Column-wise Angle Preservation Theorem

*Proof.* For any pair of column indices  $i \neq j$ , the cosines of the angles between the vectors in principal weights  $(\mathbf{w}_i^{\text{pri}}, \mathbf{w}_j^{\text{pri}})$  and the vectors in fine-tuned weights  $(\mathbf{w}_i, \mathbf{w}_j)$  are:

$$\cos \theta_{ij}^{\text{pri}} = \frac{\mathbf{b}_i^\top \mathbf{G} \mathbf{b}_j}{\sqrt{\mathbf{b}_i^\top \mathbf{G} \mathbf{b}_i} \sqrt{\mathbf{b}_j^\top \mathbf{G} \mathbf{b}_j}}, \quad \cos \theta_{ij} = \frac{\mathbf{b}_i^\top \mathbf{R}^\top \mathbf{G} \mathbf{R} \mathbf{b}_j}{\sqrt{\mathbf{b}_i^\top \mathbf{R}^\top \mathbf{G} \mathbf{R} \mathbf{b}_i} \sqrt{\mathbf{b}_j^\top \mathbf{R}^\top \mathbf{G} \mathbf{R} \mathbf{b}_j}}.$$

**Sufficiency.** If  $\mathbf{R}^\top \mathbf{G} \mathbf{R} = \mathbf{G}$ , substituting this identity into the second fraction yields  $\cos \theta_{ij} = \cos \theta_{ij}^{\text{pri}}$ . Since all angles lie in the interval  $[0, \pi]$ , where the cosine function is strictly monotonic, it follows that  $\theta_{ij} = \theta_{ij}^{\text{pri}}$ .

**Necessity.** Conversely, assume angle preservation holds, *i.e.*,  $\theta_{ij} = \theta_{ij}^{\text{pri}}$  for all  $i \neq j$ . Introduce  $\mathbf{M} := \mathbf{R}^\top \mathbf{G} \mathbf{R} - \mathbf{G}$ . The equality of the two cosine formulas implies that  $\mathbf{b}_i^\top \mathbf{M} \mathbf{b}_j = 0$  for all  $i, j$ . This condition is equivalent to  $\langle \mathbf{M}, \mathbf{b}_i \mathbf{b}_j^\top \rangle_F = 0$ , where  $\langle X, Y \rangle_F := \text{tr}(X^\top Y)$  denotes the Frobenius inner product. Since  $\text{rank}(\mathbf{B}) = r$  and there exists some pair  $i \neq j$  such that  $\mathbf{b}_i^\top \mathbf{G} \mathbf{b}_j \neq 0$ , the set of outer products  $\{\mathbf{b}_i \mathbf{b}_j^\top\}_{i,j}$  spans a nontrivial subspace of  $\mathbb{R}^{r \times r}$ . If  $\mathbf{M} \neq 0$ , there exists at least one pair  $(i, j)$  such that the Frobenius inner product  $\langle \mathbf{M}, \mathbf{b}_i \mathbf{b}_j^\top \rangle_F$  is nonzero, contradicting the orthogonality condition. Hence,  $\mathbf{M} = 0$ , and it follows that  $\mathbf{R}^\top \mathbf{G} \mathbf{R} = \mathbf{G}$ .  $\square$

## B Convergence and Stability of MOFT

This section provides a theoretical analysis of the convergence and stability of principal subspace adaptation in MOFT. Let  $L(\theta)$  denote the fine-tuning loss, and define  $L^* = \min_{\theta} L(\theta)$  as its global minimum.

Following previous works [20, 9], we assume that both the pre-trained model and its fine-tuned variant lie in a *low intrinsic rank* subspace. In particular, we suppose that the Hessian of  $L(\theta)$  is dominated by  $r$  leading singular values, meaning that the gradient  $\nabla L(\theta)$  approximately resides in an  $r$ -dimensional subspace  $\mathcal{S} \subseteq \mathbb{R}^d$ . Moreover, we assume that  $L(\theta)$  satisfies the Polyak–Łojasiewicz (PL) condition:

$$\|\nabla L(\theta)\|^2 \geq 2\mu [L(\theta) - L^*], \quad \mu > 0, \quad (10)$$

which ensures sufficient gradient magnitude whenever the current loss is above the optimum.

Let  $P_{\mathcal{S}}$  denote the orthogonal projection onto the principal subspace  $\mathcal{S}$ . Then, the gradient can be approximated as:

$$\nabla L(\theta) \approx P_{\mathcal{S}}(\nabla L(\theta)), \quad (11)$$

indicating that restricting updates to  $\mathcal{S}$  captures all major descent directions.

Combining (10) and (11), and following standard PL convergence analysis [43], we obtain the following bound using a decaying step size  $\eta_k = \frac{2k+1}{2\mu(k+1)^2}$ :

$$\mathbb{E}[L(\theta^{(k+1)}) - L^*] \leq \frac{L\sigma^2}{2\mu^2 k} \leq \frac{LC^2}{2\mu^2 k}, \quad (12)$$

where  $L$  is the Lipschitz constant of the gradient, and  $\sigma^2$  (resp.  $C^2$ ) is the variance bound of the stochastic gradient in the subspace  $\mathcal{S}$  (resp. full parameter space).

This analysis highlights that constraining updates to the principal subspace not only retains the effective descent directions but also reduces the influence of high-variance noise from irrelevant directions. As a result, MOFT benefits from improved stability and convergence behavior, despite sharing the same theoretical rate of  $O(1/k)$  with unconstrained optimization.

## C Connection between MOFT and Full-Space Orthogonal Fine-Tuning

In this section, we analyze the connection between MOFT and conventional full-space orthogonal fine-tuning by leveraging the well-known Orthogonal Complement Theorem, a classical result in linear algebra.

**Theorem C.1** (Orthogonal Complement Theorem). *Let  $\mathcal{S}$  be a subspace of an  $n$ -dimensional inner product space. Then there exists an orthogonal complement subspace  $\mathcal{S}^\perp \subseteq \mathbb{R}^d$  with  $\dim(\mathcal{S}^\perp) = d - r$ , such that*

$$\mathbb{R}^d = \mathcal{S} \oplus \mathcal{S}^\perp, \tag{13}$$

where every vector  $x \in \mathcal{S}^\perp$  is orthogonal to all vectors  $v \in \mathcal{S}$ , i.e.,  $\langle x, v \rangle = 0$ .

Let  $\{u_1, \dots, u_r\}$  be an orthonormal basis for  $\mathcal{S}$ , satisfying  $\langle u_i, u_j \rangle = \delta_{ij}$ . By Theorem C.1, we can complete this basis to span  $\mathbb{R}^d$  with  $\{u_{r+1}, \dots, u_d\}$  spanning  $\mathcal{S}^\perp$ . The combined set  $\{u_1, \dots, u_d\}$  then forms a complete orthonormal basis for  $\mathbb{R}^d$ .

In MOFT, the orthogonal transformation is applied solely to the principal subspace  $\mathcal{S}$ . This partial transformation can be lifted to the full space by defining a composite operator  $\mathbf{R}_{full}$  that acts as follows:

$$\mathbf{R}_{full}(u_i) = \begin{cases} \mathbf{R}(u_i), & 1 \leq i \leq r, \\ u_i, & r + 1 \leq i \leq n, \end{cases} \tag{14}$$

where  $\mathbf{R} \in O(r)$  is the orthogonal transformation used in MOFT. Clearly,  $\mathbf{R}' \in O(d)$  since it preserves inner products across the full space.

In matrix form, under the basis  $\{u_1, \dots, u_n\}$ , the transformation  $\mathbf{R}_{full}$  can be represented as:

$$\mathbf{R}_{full} = \begin{pmatrix} \mathbf{R} & 0 \\ 0 & \mathbf{I}_{(d-r)} \end{pmatrix}, \tag{15}$$

where  $\mathbf{R}$  applies to the principal subspace (i.e.,  $\mathbf{W}_{pri}$ ), and  $\mathbf{I}_{(d-r)}$  is the identity transformation on the residual subspace  $\mathbf{W}_{res}$ .

This formulation highlights that MOFT can be interpreted as a structured instance of full-space orthogonal fine-tuning, where the orthogonal transformation is restricted to the principal subspace, while the identity transformation is applied to its orthogonal complement. This structure significantly reduces the computational and memory overhead associated with orthogonal fine-tuning from dimensionality. Consequently, MOFT retains the advantages of orthogonal fine-tuning in a resource-efficient manner.

## D The Activation Memory Statistics across Different PEFT Methods

In this section, we analyze the activation memory requirements of various PEFT methods during fine-tuning. In transformer-based networks, memory usage primarily arises from three sources: *pre-trained weight storage*, *activation storage*, and *gradient/optimizer state storage*. Activation storage refers to intermediate values created during the forward pass and retained for gradient computation during backpropagation. Different PEFT methods consume comparable amounts of memory for weights, gradients, and optimizer states, as they all involve a substantially reduced number of trainable parameters [9, 26, 29]. In contrast, their activation memory consumption exhibits clear differences. As the batch size increases, activation storage gradually becomes the dominant memory bottleneck, as illustrated in Figure 1b. Notably, activation memory in transformer layers accounts for over 99.9% of the total activation memory across all layers [34]. We therefore focus our analysis on the activation storage of transformer layers.

In this study, we consider the transformer layers within an encoder or decoder, where the input has dimensions  $b \times s \times h$ , where  $b$  denotes the micro-batch size,  $s$  represents the maximum sequence length, and  $h$  indicates the hidden dimension size. Each transformer layer consists of a self-attention layer with  $a$  attention heads, and in the feed-forward network (FFN) layer, the hidden dimension is expanded to  $4h$  before being projected back to  $h$ . We assume that activations are stored in 32-bit floating-point format, requiring 4 bytes of memory. All results in this section are reported in bytes unless otherwise specified.

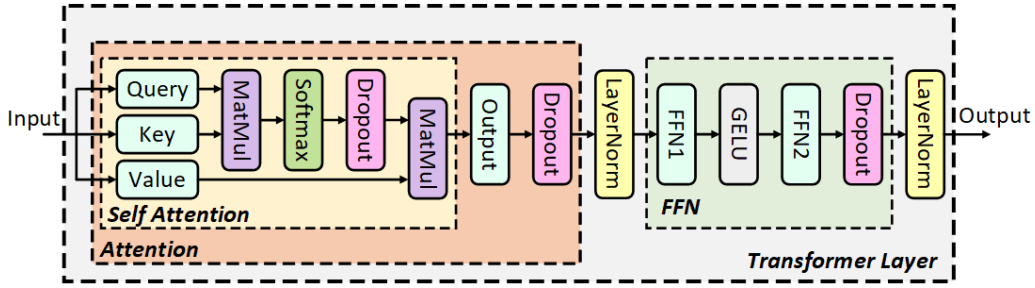


Figure 4: The architecture of a single transformer layer, including the attention layer and the feed forward network layer and self attention layer.

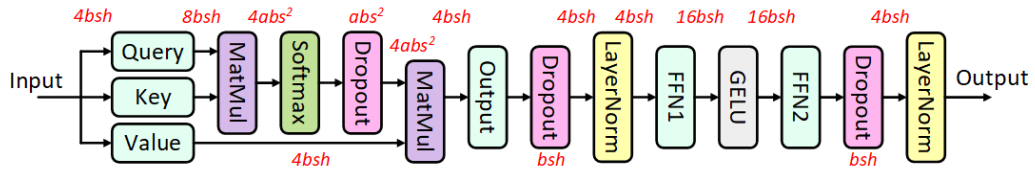


Figure 5: Activation memory statistics in a single transformer layer for full fine-tuning.

As illustrated in Figure 4, each transformer layer consists of a self-attention block (including Query, Key, and Value matrices) combined with an output linear layer to form the attention block. Additionally, it includes two FFN layers, two normalization layers, and three dropout layers. Building on prior work [34], we derive an approximate formula for the activation memory required during the forward pass of a single transformer layer. For backpropagation, we consider the input of each module (which serves as the output for the subsequent module) as activations. As illustrated in Figure 5, the activation memory includes the following components:

**Self-Attention:**

- Query ( $Q$ ), Key ( $K$ ), and Value ( $V$ ) matrices: Require  $4bsh$  for their shared inputs.
- First MatMul: Requires  $8bsh$  as input to the module.
- Softmax: Requires  $4abs^2$  for activation storage.
- Self-attention dropout: Only the mask is stored, with a size of  $abs^2$ .
- Second MatMul: Requires activations from the output of dropout ( $4abs^2$ ) and linear layer Value ( $4bsh$ ), totaling  $4abs^2 + 4bsh$ .

**Attention:**

- Output linear layer: Requires  $4bsh$  as input.
- Attention dropout: Only the mask is stored, with a size of  $bsh$ .
- First layer normalization: Requires  $4bsh$  for activation storage.

**FFN:**

- FFN1: Requires  $4bsh$  as input.
- GELU activation: Requires  $16bsh$  for activation storage.
- FFN2: Requires  $16bsh$  as input.
- FFN dropout: Only the mask is stored, with a size of  $bsh$ .
- Second layer normalization: Requires  $4bsh$  for activation storage.

Summing these sub-layers, the total activation storage for a single transformer layer is:

$$ACT_{base} = 66bsh + 9abs^2 \tag{16}$$

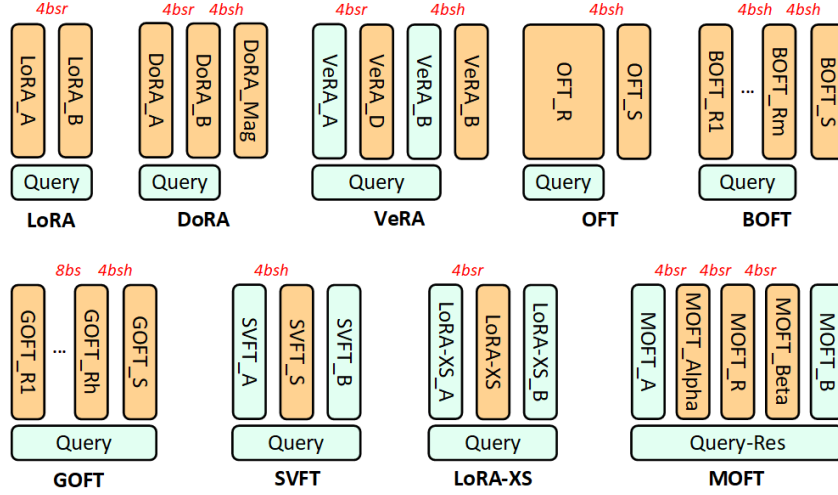


Figure 6: Activation memory statistics in a single linear layer (Query) across different PEFT methods.

Table 6: Total activation memory statistics in a single transformer layer for different PEFT methods and FFT. In BOFT,  $m$  denotes the number of sparse matrices.

Methods	Activation memory (Relative)	Activation memory (Absolute)
FFT	$ACT_{base}$	$66bsh + 9abs^2$
LoRA	$ACT_{base} + 24bsr$	$66bsh + 24bsr + 9abs^2$
DoRA	$ACT_{base} + 24bsr + 36bsh$	$102bsh + 24bsr + 9abs^2$
VeRA	$ACT_{base} - 28bsh + 16bsr + 36bsh$	$74bsh + 16bsr + 9abs^2$
OFT	$ACT_{base} + 36bsh$	$102bsh + 9abs^2$
BOFT	$ACT_{base} + 36mbsh$	$66bsh + 36mbsh + 9abs^2$
GOFT	$ACT_{base} + 108bsh - 48bs$	$174bsh + 9abs^2 - 48bs$
SVFT	$ACT_{base} - 28bsh + 24bsh$	$62bsh + 9abs^2$
LoRA-XS	$ACT_{base} - 28bsh + 24bsr$	$38bsh + 24bsr + 9abs^2$
MOFT	$ACT_{base} - 28bsh + 72bsr$	$38bsh + 72bsr + 9abs^2$

The six linear layers within a transformer layer undergo changes in activation memory storage when different PEFT methods are applied, as reflected by modifications to the base formula ( $ACT_{base}$ ). For example, the LoRA method introduces a set of low-rank matrices  $B$  and  $A$  in parallel. The activation memory requirements for various PEFT methods in a single linear layer are summarized in Figure 6, with the Query matrix as a representative example. The specific details of these changes are as follows:

- **LoRA**: Adds  $4bsr$  to the original activation storage for gradient computation during back-propagation.
- **DoRA**: Adds  $4bsr + 4bsh$  to the original activation storage.
- **VeRA**: Replaces the original input  $4bsh$  with  $4bsr$  and adds  $4bsh$  for activation storage.
- **OFT**: Adds  $4bsh$  to the original activation storage.
- **BOFT**: Requires an additional  $4mbsh$ , where  $m$  is the number of sparse matrices.
- **GOFT**: Adds  $(h - 1)8bs + 4bsh = 12bsh - 8bs$ , where  $h$  is the hidden layer dimension.
- **SVFT**: Removes the original input activation storage and adds  $4bsh$ .
- **LoRA-XS**: Removes the original input activation storage and adds  $4bsr$ .
- **MOFT**: Removes the original input activation storage and adds  $12bsr$ .

The activation memory requirements of various PEFT methods for a single transformer layer are summarized in Table 6. Notably, MOFT incurs significantly lower activation memory than all other methods except LoRA-XS. Its activation memory is comparable to that of LoRA-XS, as the rank  $r$  is much smaller than the hidden dimension  $h$  ( $r \ll h$ ). A key observation is that MOFT employs scale vectors to enhance task-specific flexibility, similar to other orthogonal fine-tuning methods [11, 13, 14]. However, unlike these methods, MOFT applies the scale vectors within a principal subspace, effectively preventing a substantial increase in activation memory usage.

## E Cayley Parameterization

The Cayley parameterization [35] is a mapping that converts real skew-symmetric matrices into orthogonal matrices. For a real skew-symmetric matrix  $A$  (i.e.,  $A^\top = -A$ ), the Cayley transform is defined as:

$$C = (I - A)(I + A)^{-1},$$

where  $I$  is the identity matrix of the same size as  $A$  and matrix  $C$  does not have -1 as an eigenvalue.

The Cayley transform provides a way to parameterize orthogonal matrices near the identity matrix using skew-symmetric matrices. The orthogonality of the Cayley transform is proved as follows.

**Theorem E.1.** *If  $A$  is a real skew-symmetric matrix and  $(I + A)$  is invertible, then the Cayley transform  $C = (I - A)(I + A)^{-1}$  is an orthogonal matrix.*

*Proof.* We aim to prove that the matrix  $C$  after Cayley transform satisfies  $C^\top C = CC^\top = I$ .

To compute  $C^\top C$ :

$$\begin{aligned} C^\top C &= ((I - A)(I + A)^{-1})^\top ((I - A)(I + A)^{-1}) \\ &= ((I + A)^{-1})^\top (I - A)^\top (I - A)(I + A)^{-1} \\ &= ((I + A)^\top)^{-1} (I - A)^\top (I - A)(I + A)^{-1} \end{aligned}$$

By the definition of skew-symmetry,  $A^\top = -A$ ,

$$= (I - A)^{-1} (I + A)(I - A)(I + A)^{-1}$$

Since  $(I + A)$  and  $(I - A)$  are commute, we can switch the order of the factors:

$$\begin{aligned} &= (I - A)^{-1} (I - A)(I + A)(I + A)^{-1} \\ &= I \end{aligned}$$

Similarly, it can be proven that  $CC^\top = I$ . Therefore, the result of Cayley transform  $C = (I - A)(I + A)^{-1}$  is an orthogonal matrix.  $\square$

In this paper, MOFT leverages the Cayley parameterization to construct orthogonal matrices with approximately half the number of trainable parameters compared to a full orthogonal matrix, while rigorously preserving orthogonality.

## F Comparison of Trainable Parameters for PEFT Methods

Table 7 compares the number of trainable parameters across representative PEFT methods. Most existing methods scale their parameter count with the hidden layer dimensions, which limits their applicability to larger models. In contrast, both MOFT and LoRA-XS decouple the number of trainable parameters from layer width. MOFT further reduces parameter complexity by adopting the Cayley parameterization, which requires only  $r(r - 1)/2$  parameters to represent an orthogonal matrix. The total number of trainable parameters in MOFT remains constant for a given rank  $r$ , enabling fine-grained control over parameter budgets. Additionally, two learnable scaling vectors are introduced within the subspace, contributing only  $2r$  additional parameters—negligible compared to other methods.

Table 7: Comparison of trainable parameters for different PEFT methods within a single linear layer, assuming input/output dimensions  $d$  and  $n$ , respectively. Here,  $r$  denotes the low-rank dimension,  $m$  the number of butterfly factors in BOFT,  $b$  the block size in BOFT,  $d_{\min} = \min(d, n)$ , and  $k$  the number of additional off-diagonals in SVFT. All statistics are based on implementations from the HuggingFace’s PEFT library [44].

Method	Number of Trainable Parameters
LoRA	$d \times r + r \times n$
DoRA	$d \times r + r \times n + n$
VeRA	$r + n$
OFT	$r \times (d/r) \times (d/r) + n$
BOFT	$m \times (d/b) \times b^2 + n$
SVFT	$d_{\min} \times k + (d_{\min} - k)(k + 1)$
LoRA-XS	$r \times r$
MOFT (Ours)	$r(r - 1)/2 + 2r$

## G Commonsense Reasoning on Commonsense-15K

### G.1 Datasets

Commonsense reasoning benchmarks encompass eight distinct sub-tasks: BoolQ [45], PIQA [46], SIQA [47], HellaSwag [48], Winogrande [49], ARC-easy/ARC-challenge [50], and OpenBookQA [51]. Following the approach described in [36, 27, 10], we also combine the training datasets from all eight tasks to construct a unified fine-tuning dataset-Commonsense-15K tailored for each task.

Table 8: Hyperparameter settings for fine-tuning on Commonsense-15K

Hyperparameter	LLaMA-3.1-8B
Optimizer	AdamW
Warmup Steps	100
LR Schedule	Linear
Max Seq. Len.	512
Batch Size	64
# Epochs	3
LR MOFT <sub><math>r=72</math></sub>	1E-03
LR MOFT <sub><math>r=184</math></sub>	4E-04

### G.2 Implementation Details

The experiments are conducted based on the frameworks established in [36, 10], utilizing PyTorch [52] and the Huggingface’s PEFT library [44]. Following the settings of [27], we only adjust the learning rates for different models. For experiments with LLaMA-3.1-8B as shown in Table 1, we adapt the  $Q, K, V, U, D$  modules for all baselines except BOFT <sub>$m=2$</sub>  <sup>$b=2$</sup>  and LoRA <sub>$r=1$</sub> . Specifically, BOFT is applied to the  $Q, V$  modules due to the high computational cost of extending it to multiple modules. Meanwhile, LoRA <sub>$r=1$</sub>  is applied to the  $Q, K, V$  modules to align with the reduced trainable parameter numbers of methods such as MOFT, SVFT, and LoRA-XS. Detailed hyperparameter configurations used in the experiments are provided in Table 8.

## H Mathematical Question Answering on MetaMathQA-40K

### H.1 Datasets

For mathematical question answering tasks, we fine-tune baselines and MOFT using the MetaMathQA-40K dataset [37] and evaluate their performance on the two challenge benchmarks: GSM-8K [40] and MATH [41].

Table 9: Hyperparameter settings for fine-tuning on MetaMathQA-40K

Hyperparameter	LLaMA-3.2-3B
Optimizer	AdamW
Warmup Ratio	0.1
LR Schedule	Cosine
Max Seq. Len.	512
Batch Size	64
# Epochs	2
LR MOFT <sub>r=72</sub>	8E-04
LR MOFT <sub>r=152</sub>	4E-04

### H.2 Implementation Details

Our experiments follow prior work [13, 27] and are implemented in PyTorch [52] using Huggingface’s PEFT library [44]. Following [27], we tune only the learning rates for different models. For LLaMA-3.2-3B, MOFT and all baselines are applied to the  $Q, K, V, U, D, O, G$  modules, except BOFT<sub>m=2</sub><sup>b=2</sup> and LoRA<sub>r=1</sub>. Due to its high resource demands, BOFT is limited to  $Q, K, V$ ; LoRA<sub>r=1</sub> is also applied to these modules to match the reduced parameter count of MOFT, SVFT, and LoRA-XS. For LLaMA-3.1-8B, MOFT and baselines are applied to  $Q, K, V, U, D$ , while BOFT is restricted to  $Q, V$ . Detailed hyperparameters are listed in Table 9.

## I Natural Language Understanding on GLUE

### I.1 Datasets

The General Language Understanding Evaluation (GLUE) [15] is a comprehensive benchmark for evaluating the performance of natural language understanding (NLU) models across diverse tasks. It includes one text similarity task (SST-B), five pairwise text classification tasks (MNLI, RTE, QQP, MRPC, and QNLI), and two single-sentence classification tasks (CoLA and SST).

Table 10: Hyperparameter settings for fine-tuning DeBERTaV3-base on GLUE

Hyperparameter	MNLI	SST-2	MRPC	CoLA	QNLI	QQP	RTE	STS-B
Optimizer				AdamW				
Warmup Ratio				0.1				
LR Schedule				Linear				
Learning Rate (Head)				5E-04				
Batch Size				32				
Dropout				5E-02				
Max Seq. Len.	256	128	320	64	512	320	320	128
#Epochs	10	10	30	30	10	10	30	20
LR MOFT <sub>r=48</sub>	1E-04	1E-04	4E-04	5E-04	2E-04	3E-04	5E-04	5E-04
LR MOFT <sub>r=144</sub>	5E-05	6E-05	2E-04	6E-05	5E-05	1E-04	2E-04	5E-05

## I.2 Implementation Details

The experiments are implemented based on the open-source LoRA [9], leveraging PyTorch [52] and the Huggingface’s PEFT library [44]. We follow the settings of [13] and only tune model-agnostic hyperparameters, such as learning rates and training epochs. MOFT is applied to all linear layers of the DeBERTaV3-base model. Metrics include matched accuracy for MNLI, Matthew’s correlation for CoLA, Pearson correlation for STS-B, and accuracy for other sub-datasets. Detailed hyperparameter configurations used in the experiments can be found in Table 10.

## J Visual Classification on VTAB-1K

### J.1 Datasets

The Visual Task Adaptation Benchmark (VTAB-1K) [16] comprises 19 image classification tasks grouped into three categories: natural, specialized, and structured.

- **Natural tasks** involve images captured with standard cameras, depicting scenes from the natural environment, generic objects, fine-grained categories, or abstract concepts.
- **Specialized tasks** use images obtained through specialized equipment, such as medical imaging devices or remote sensing technologies.
- **Structured tasks** focus on artificially designed scenarios to analyze specific relationships or changes between images, such as estimating object distances in 3D scenes (e.g., DMLab), counting objects (e.g., CLEVR), or detecting orientations (e.g., dSprites for disentangled representations).

In VTAB-1K, each dataset provides 800 labeled samples from its original training set, which are used to fine-tune the base model. Additionally, 200 labeled samples in the validation set adjust hyperparameters during fine-tuning. The performance is evaluated using Top-1 classification accuracy on the respective original test set.

Table 11: Hyperparameter settings for fine-tuning ViT-B/16 on VTAB-1K

Hyperparameter	ViT-B/16
Optimizer	AdamW
Warmup Ratio	0.1
LR Schedule	Cosine
Learning Rate (Head)	5E-03
Batch Size	64
Weight Decay	1E-03
Dropout	1E-01
#Epochs	50
LR MOFT <sub>r=48</sub>	{5E-04, 1E-03, 5E-03}
LR MOFT <sub>r=184</sub>	{1E-04, 5E-04, 1E-03}

### J.2 Implementation Details

Our experiments are implemented in PyTorch [52] using HuggingFace’s `Datasets`, `Transformers`, and `PEFT` [44] libraries. In contrast to prior works that rely on the `Timm` framework with custom preprocessing and training loops [13, 14], our framework adopts standardized APIs such as `AutoImageProcessor` and `Trainer`, removing the need for manual dataset/model handling and enabling fast integration of advanced methods (e.g., DoRA [10], SVFT [27], BOFT [13]).

We follow the experimental settings in [13, 14], adjusting learning rates, weight decay, and training epochs accordingly. Following [26, 27, 29], we also separate learning rates for the classification head and PEFT modules, with a fixed learning rate applied to the head across all methods. Full hyperparameter details are provided in Table 11.

## K Computational Cost Comparisons

We evaluate the computational overhead of MOFT compared to baseline methods on ViT-B/16 [16] and the larger LLaMA-3.2-3B [18] models. All experiments are conducted on a single NVIDIA RTX 4090 (24GB) and a single NVIDIA H100 (80GB) GPU, using the same hyperparameter settings as described in Appendix H and Appendix J.

Table 12: Training throughput (samples per second) comparison using ViT-B/16 on the VTAB-1K benchmark.

Methods	Training Samples per Second
FFT	137.80
LoRA <sub>r=8</sub>	144.51
DoRA <sub>r=8</sub>	98.20
VeRA <sub>r=1024</sub>	96.80
BOFT <sub>m=2</sub> <sup>b=2</sup>	85.80
SVFT <sub>P</sub>	118.19
LoRA-XS <sub>r=32</sub>	128.25
MOFT <sub>r=48</sub>	102.66

For the relatively small ViT-B/16 model, as shown in Table 12, MOFT achieves higher training throughput (samples per second) than DoRA, VeRA, and BOFT, owing to its orthogonal transformations being confined to the principal subspace. However, MOFT still incurs approximately 1.4× the computational cost of LoRA, primarily due to the overhead introduced by Cayley parameterization.

As model size increases, Table 13 shows that both BOFT and MOFT incur higher training times than LoRA on LLaMA-3.2-3B due to the inherent limitation of orthogonal parameterization. Nevertheless, MOFT achieves a 30%–60% speedup over BOFT under the same module insertion configuration. This is attributed to MOFT’s efficient design, which restricts the Cayley transform to the  $r$ -dimensional subspace, substantially reducing memory and computational costs compared to full-space orthogonal fine-tuning. As a result, MOFT scales more favorably with model size than BOFT.

Table 13: Training throughput (samples per second) comparison using LLaMA-3.2-3B on MetaMathQA-40K.

Methods	Inserted Modules	Training Samples per Second
LoRA <sub>r=1</sub>	Q, K, V, U, D, O, G	21.55
BOFT <sub>m=2</sub> <sup>b=2</sup>	Q, K, V	11.55
BOFT <sub>m=4</sub> <sup>b=4</sup>	Q, K, V	7.77
MOFT <sub>r=72</sub>	Q, K, V, U, D, O, G	11.90
MOFT <sub>r=72</sub>	Q, K, V	17.51

Table 14: Runtime comparison using LLaMA-3.2-3B on MetaMathQA-40K.

Methods	Inserted Modules	Runtime (min)
LoRA <sub>r=1</sub>	Q, K, V, U, D, O, G	57
BOFT <sub>m=2</sub> <sup>b=2</sup>	Q, K, V	111
BOFT <sub>m=4</sub> <sup>b=4</sup>	Q, K, V	173
MOFT <sub>r=72</sub>	Q, K, V, U, D, O, G	98 (SVD <2)
MOFT <sub>r=72</sub>	Q, K, V	74 (SVD <2)

We further evaluate the runtime cost of MOFT, including the one-time SVD step. As shown in Table 14, the SVD operation accounts for less than 3% of the total fine-tuning time and can be further

accelerated using fast SVD algorithms [33, 12]. These runtime results align well with the training throughput trends observed in Table 13.

While MOFT introduces moderately higher computational overhead than LoRA, it consistently offers superior parameter efficiency across a wide range of models and tasks, making the trade-off acceptable in practice (see Section 5 of the main paper). Unlike BOFT, which relies on custom CUDA-level optimization, our MOFT implementation uses only standard PyTorch operations without hardware-specific tuning, leaving ample room for future runtime improvements. In future work, we plan to incorporate Sparse Matrix Multiplications (SpMM) and leverage highly optimized numerical libraries to further reduce the computational cost of orthogonal operations.

## L Extension Experiments

### L.1 Effect of SVD initialization

MOFT constructs the principal subspace via SVD, where the initialization time and accuracy of fast SVD depend on the `n_iter` parameter [33, 12]. We evaluate this on the Commonsense-15K dataset [36] using the LLaMA-3.2-3B model [18], reporting both initialization time and validation loss. As shown in Table 15, smaller `n_iter` values yield faster initialization while increasing `n_iter` improves accuracy. With `n_iter = 20`, the loss closely matches that of full SVD (`n_iter → ∞`). These results confirm that fast SVD initializes MOFT in seconds, and even full SVD adds negligible overhead relative to total fine-tuning time.

Table 15: The effect of SVD Initialization on the Commonsense-15K Dataset using the LLaMA-3.2-3B model.

Methods	SVD $n\_iter$	SVD Init Time	Validation Loss
MOFT <sub><math>r=32</math></sub>	5	2.79	0.9343
	10	3.74	0.9328
	20	4.84	0.9283
	$\infty$	89.68	0.9276
MOFT <sub><math>r=64</math></sub>	5	4.11	0.9174
	10	5.13	0.9134
	20	7.51	0.9157
	$\infty$	89.48	0.9147
MOFT <sub><math>r=128</math></sub>	5	6.33	0.9092
	10	8.38	0.9028
	20	13.01	0.9029
	$\infty$	90.50	0.8992

### L.2 Effect of ranks

To provide guidance on rank selection and evaluate the effect of ranks on performance, we conduct experiments with rank configurations ranging from 1 to 256 on the Commonsense-15K dataset [36] using the LLaMA-3.2-3B model [18]. As shown in Table 16, the performance of MOFT generally improves with increasing rank, indicating that MOFT significantly benefits from larger parameter budgets. However, the accuracy gains diminish as the rank continues to grow, showing the importance of finding a balance between the number of parameters and performance. Importantly, despite the substantial increase in the number of parameters, the peak memory usage of MOFT shows only a marginal increase. This is due to the unique structure of MOFT, which fine-tunes only a compact  $r \times r$  orthogonal matrix.

## M Standard Deviations on GLUE and VTAB-1K Benchmarks

To assess statistical significance, we report standard deviations over five runs with different random seeds for both natural language understanding (GLUE [15]) and visual classification (VTAB-1K [16]),

Table 16: Effects of different ranks fine-tuned on the Commonsense-15K Dataset using the LLaMA-3.2-3B model.

Methods	Ranks	#Params	Peak GPU Memory (GB)	Avg. (%)
MOFT	1	352	31.46	27.07
	4	2,744	31.49	36.16
	8	8,624	31.52	38.21
	16	29,792	31.60	57.12
	32	109,760	31.75	62.94
	64	420,244	32.07	70.95
	128	1,643,264	32.81	73.90
	256	6,497,792	34.47	74.95

as shown in Table 17 and Table 18. These values correspond to the results reported in the main paper and quantify variability due to random initialization and training dynamics.

Table 17: Standard deviations corresponding to the main results in Table 3. Results are computed over 5 runs with different random seeds.

Methods	MNLI	SST-2	MRPC	CoLA	QNLI	QQP	RTE	STS-B
LoRA-XS <sub>r=32</sub>	$\pm 0.15$	$\pm 0.20$	$\pm 0.37$	$\pm 0.92$	$\pm 0.10$	$\pm 0.12$	$\pm 0.60$	$\pm 0.15$
MOFT <sub>r=48</sub>	$\pm 0.06$	$\pm 0.17$	$\pm 0.54$	$\pm 0.75$	$\pm 0.13$	$\pm 0.10$	$\pm 0.99$	$\pm 0.11$
MOFT <sub>r=144</sub>	$\pm 0.06$	$\pm 0.15$	$\pm 0.37$	$\pm 0.48$	$\pm 0.15$	$\pm 0.10$	$\pm 1.16$	$\pm 0.16$

Table 18: Standard deviations corresponding to the main results in Table 4. Results are computed over 5 runs with different random seeds.

Methods	Natural							Specialized				Structured							
	Cifar100	Caltech101	DTD102	Flower102	Pets	SVHN	Sun397	Camelyon	EuroSAT	Resisc45	Retinopathy	Clevr-Count	Clevr-Dist	DMLab	KITTI-Dist	dSpr-Loc	dSpr-Ori	sNOBB-Azim	sNOBB-Ele
FFT	$\pm 0.50$	$\pm 1.04$	$\pm 0.74$	$\pm 0.21$	$\pm 0.67$	$\pm 0.68$	$\pm 0.50$	$\pm 0.82$	$\pm 1.13$	$\pm 0.71$	$\pm 1.72$	$\pm 3.80$	$\pm 0.71$	$\pm 2.07$	$\pm 2.53$	$\pm 2.41$	$\pm 1.64$	$\pm 0.39$	$\pm 0.88$
LoRA <sub>r=8</sub>	$\pm 0.86$	$\pm 0.19$	$\pm 1.08$	$\pm 0.14$	$\pm 0.32$	$\pm 1.80$	$\pm 0.11$	$\pm 0.36$	$\pm 0.51$	$\pm 0.57$	$\pm 0.45$	$\pm 1.95$	$\pm 1.51$	$\pm 1.62$	$\pm 1.25$	$\pm 3.54$	$\pm 0.78$	$\pm 0.62$	$\pm 1.28$
DoRA <sub>r=8</sub>	$\pm 0.81$	$\pm 0.20$	$\pm 0.58$	$\pm 0.17$	$\pm 0.23$	$\pm 1.85$	$\pm 0.12$	$\pm 0.52$	$\pm 0.41$	$\pm 0.13$	$\pm 0.72$	$\pm 3.89$	$\pm 2.06$	$\pm 1.16$	$\pm 1.16$	$\pm 2.35$	$\pm 0.49$	$\pm 0.61$	$\pm 0.85$
BOFT <sub>m=2</sub>	$\pm 1.55$	$\pm 1.37$	$\pm 1.40$	$\pm 0.29$	$\pm 0.73$	$\pm 1.03$	$\pm 0.58$	$\pm 1.46$	$\pm 1.16$	$\pm 1.53$	$\pm 1.71$	$\pm 2.24$	$\pm 0.96$	$\pm 1.03$	$\pm 2.22$	$\pm 1.96$	$\pm 1.29$	$\pm 0.82$	$\pm 1.02$
SVFT <sub>P</sub>	$\pm 0.34$	$\pm 0.33$	$\pm 0.24$	$\pm 0.13$	$\pm 0.38$	$\pm 0.99$	$\pm 0.62$	$\pm 0.52$	$\pm 0.41$	$\pm 0.51$	$\pm 0.70$	$\pm 1.04$	$\pm 1.14$	$\pm 0.80$	$\pm 1.76$	$\pm 1.48$	$\pm 0.82$	$\pm 0.79$	$\pm 0.63$
LoRA-XS <sub>r=32</sub>	$\pm 0.90$	$\pm 0.82$	$\pm 0.61$	$\pm 0.12$	$\pm 0.54$	$\pm 0.44$	$\pm 0.23$	$\pm 0.38$	$\pm 0.22$	$\pm 0.34$	$\pm 0.42$	$\pm 2.54$	$\pm 1.39$	$\pm 0.79$	$\pm 1.71$	$\pm 0.94$	$\pm 0.73$	$\pm 0.80$	$\pm 0.61$
Fact-IT <sub>r=16</sub>	$\pm 0.39$	$\pm 0.40$	$\pm 0.27$	$\pm 0.06$	$\pm 0.17$	$\pm 0.92$	$\pm 0.08$	$\pm 0.23$	$\pm 0.24$	$\pm 0.21$	$\pm 0.32$	$\pm 0.40$	$\pm 0.42$	$\pm 0.39$	$\pm 1.14$	$\pm 1.07$	$\pm 0.56$	$\pm 0.35$	$\pm 0.62$
Fact-TK <sub>r=32</sub>	$\pm 0.21$	$\pm 0.24$	$\pm 0.35$	$\pm 0.07$	$\pm 0.23$	$\pm 0.51$	$\pm 0.23$	$\pm 1.04$	$\pm 0.20$	$\pm 0.41$	$\pm 0.56$	$\pm 0.41$	$\pm 0.43$	$\pm 0.22$	$\pm 1.10$	$\pm 1.09$	$\pm 0.78$	$\pm 0.19$	$\pm 0.92$
MOFT <sub>r=48</sub>	$\pm 1.01$	$\pm 1.01$	$\pm 0.69$	$\pm 0.13$	$\pm 0.35$	$\pm 1.36$	$\pm 0.88$	$\pm 2.58$	$\pm 0.66$	$\pm 0.26$	$\pm 0.88$	$\pm 1.67$	$\pm 0.47$	$\pm 1.22$	$\pm 1.27$	$\pm 0.93$	$\pm 0.96$	$\pm 0.52$	$\pm 0.60$
MOFT <sub>r=184</sub>	$\pm 0.81$	$\pm 0.20$	$\pm 0.58$	$\pm 0.17$	$\pm 0.23$	$\pm 1.85$	$\pm 0.12$	$\pm 0.52$	$\pm 0.41$	$\pm 0.13$	$\pm 0.72$	$\pm 3.89$	$\pm 2.06$	$\pm 1.16$	$\pm 1.16$	$\pm 2.35$	$\pm 0.49$	$\pm 0.61$	$\pm 0.85$